UNIVERSITY OF TARTU
Faculty of Science and Technology
Institute of Ecology and Earth Sciences
Department of Geology

Hele-Riin Juhkama

Mn-carbonates in carbonate-shale succession in Palaeoproterozoic Lastoursville sub-basin, Gabon

MSc thesis

Supervisor: Kalle Kirsimäe

TARTU 2020

Mn-carbonates in carbonate-shale succession in Palaeoproterozoic Lastoursville sub-basin, Gabon

Manganese is a redox-sensitive element capable of recording paleoenvironmental information and is often used to interpret redox-conditions of the early Earth. Manganese-rich sediments appear first time in sedimentary record during the oxygenation of the Earth's atmosphere. This thesis aimed at the petrographical, mineralogical and geochemical characterization and development of Mn-bearing carbonates of the LST12 core in Lastoursville sub-basin in Palaeoproterozoic Francevillian Basin. Geochemical and mineralogical composition of the Mn-carbonates and trace element enrichments were used to determine the redox conditions and paleoenvironmental changes during the deposition of Mn-bearing carbonates and black-shales.

P420 petrology, mineralogy, geochemistry

Francevillian basin, Mn-carbonates, black shales, trace elements

Mn-karbonaatide moodustumine Paleoproterosoikumi Lastoursville alam-basseini karbonaatide ja mustade kiltade läbilõikes

Mangaan on redokstundlik element, mis salvestab endas informatsiooni paleokeskkonna kohta ning mida on laialdaselt kasutatud Maa settekeskkondade redokstingimuste rekonstrueerimiseks. Käesoleva uurimistöö eesmärgiks oli iseloomustada Lastoursville alam-basseini LST12 puursüdamiku Mn-karbonaatide petrograafiat, mineraloogilist ja geokeemilist koostist Paleoproterosoikumi Franceville basseinis. Mn-karbonaatide keemilise ja mineraloogilise koostise ning jälgelementide rikastumiste põhjal interpreteeriti redokstingimuste ja paleokeskkonna muutusi Mn-karbonaatide ja mustade kiltade moodustumisel.

P420 petroloogia, mineraloogia, geokeemia

Franceville bassein, Mn-karbonaadid, mustad kildad, jälgelemendid

Table of Contents

Introduction

Manganese, an abundant component of the Earth's crust and critical industrial metal, is geochemically significant for (paleo-)environmental interpretations in several ways. Firstly, manganese precipitates store information about the composition of fluids they have been exposed to as they readily adsorb different metals (Cu, Pb, Zn, Ba etc.) and complex ions carried in fluids. Secondly, different redox states of manganese give opportunity to constrain the history of oxidation and fluctuations in redox conditions at the Earth's surface (Kuleshov & Maynard, 2019).

Precipitation of manganese occurs in oxidized form, either as Mn (III) or Mn (IV) that can form different oxide and oxyhydroxide phases (Johnston et al., 2016). As a result, the deposition of manganese rich sediments in geological history of the Earth has been linked to the oxygenation of its surface environments. The largest sedimentary manganese deposits worldwide were formed right after the first extensive increase in atmosphere oxygen content, so called Great Oxidation Event (GOE, Holland, 2006), which occurred in the beginning of Proterozoic at about 2.4 Ga (Bekker et al., 2004; Gumsley et al., 2017). The Proterozoic manganese deposits, particularly these in modern Africa, are the largest and often associated to banded iron-ore formations (BIF), precipitation of which is also dependent on the oxidation state of iron (Kuleshov & Maynard, 2019). Manganese enrichments in sedimentary deposits can be also hosted in carbonate phases. In the presence of high concentrations of soluble Mn^{2+}, the carbonate minerals with high Mn level can form under anoxic conditions. Alternatively, the Mn-enriched carbonate minerals can precipitate within sediments due to the diagenetic reduction of Mn(III,IV)oxyhydroxides (Wittkop et al., 2020).

The Palaeoproterozoic Francevillian volcanoclastic-sedimentary succession is unique for its large sedimentary manganese ore deposits and natural uranium reactors of Oklo and Bangombé (Gauthier-Lafaye & Weber, 2003). The manganese deposits in Francevillian basin are, however, of secondary origin and formed by Cainozoic tropical weathering of primary manganese bearing rocks – Mn-rich carbonaceous shales that occur in the middle-upper part of the Palaeoproterozoic succession of the Francevillian basin (Gauthier-Lafaye & Weber, 2003). The Francevillian basin is also known for one of the best preserved Palaeoproterozoic successions that hosts the earliest discovered complex consortia of organized bacterial organisms, pre-dating by 1 Ga the rise of eukaryotic life (Moussavou et al., 2015). Because of the presence uranium and manganese ores and therefore its economic significance, the Francevillian succession has been widely studied (Reynaud et al., 2018; Gauthier-Lafaye &

Weber, 2003; Azzibrouck, 1986; Pambo, 2004). Most of these studies focus on the manganese ore, its general geology and mineralogy-geochemistry but also the geology and Mn-mineralization in the ore protolith, the Mn-carbonate bearing shales has been addressed in several studies (Azzibrouck, 1986; Pambo, 2004; Dubois, 2017).

Sediments of the Francevillian Group have undergone only minor deformation and metamorphism, which makes it an excellent study site for interpretation of primary sedimentary conditions and diagenetic changes in mineralogy and geochemistry of these carbonates. Hence, these deposits can give us valuable information about the paleoenvironmental changes and events in Earth's history (Dubois et al., 2015; Reynaud et al., 2018).

The overall goal of this thesis is to study the petrographical, mineralogical and geochemical composition of the Mn-bearing carbonates from the upper part of Francevillian Group recovered in LS12 drill-core in Lastoursville sub-basin that includes an interval of Mn-bearing dolostone and black shale. The specific aims of the study are, firstly, to document the development of chemical and mineralogical composition of carbonates in LST12 core succession. Secondly, to determine the changes in depositional palaeoenvironment and redox conditions during the genesis of Mn-bearing carbonates and black shales.

Geological setting

The Palaeoproterozoic Francevillian basin is located in the southeast of Gabon on the western margin of the Congo Craton (Figure 1) and covers an area of ~42000 km^2 (Weber & Gauthier-Lafaye, 2013; Dubois et al., 2017). About 2 km thick Francevillian unmetamorphosed volcanoclastic-sedimentary Group lies unconformably on the Archean granitoid-greenstone basement (Ossa Ossa et al., 2013; Bankole et al., 2016). The Archean basement is formed by the North Gabon Massif in the north and the Chaillu Massif in the south (Dubois et al., 2017). The Francevillian basin is an NW-SE trending horst and graben structure and it is limited with the West African Central Belt (WCAB) in the west and is covered by Meso-Cenozoic sands of Batékés plateau in the east (Dubois et al., 2015, 2017).

The basin is subdivided into four sub-basins: Booué, Lastoursville, Okondja and Franceville; and into five stratigraphic units: FA, FB, FC, FD and FE (Ossa Ossa et al., 2013). Based on the U-Pb zircon dating of N'goutou Complex granites in the Francevillian Okondja sub-basin, the minimum depositional age for FA and FB succession is of 2191±13 Ma (Sawaki et al., 2017). The U-Pb zircon date of a welded ignimbrite tuff in FD Formation from the Lastoursville sub-basin shows age of 2083±6 Ga (Horie et al., 2005) and delimits the youngest age of the succession.

The stratigraphically lowest formation FA lies unconformably over the Archean granitoid basement. It consists mainly of fine to coarse sandstones and conglomerates with interlayering mudstones. Their formation have been interpreted as fluvial to deltaic system (Bankole et al., 2016). The thickness of this unit is 100–1000 m (Ndongo et al., 2016). The upper part of the FA Formation hosts the natural nuclear reactors of the Oklo, Okélobondo and Bangombé uranium ore bodies (Mouélé et al., 2014).

The FB Formation is 300–1000 m thick (Weber & Gauthier-Lafaye, 2013) unit in the centre of the Francevillian basin and is mostly composed of sandstones and black shales/siltstones with marine depositional setting (Bankole et al., 2016). It is divided into two sub-units: FB1 and FB2. The FB1 subunit is mostly made up of carbonate rich shales (ampelites) with dolomite/manganiferous carbonates and manganese oxyhydroxides in the upper part. The FB2 is mainly represented by massive, fine-grained Poubara sandstones, that are capped by organic-rich ampelites. This subunit is interpreted as turbititic, deltaic or storm-wave deposits (Ndongo et al., 2016; Dubois et al., 2017). From the upper part of the FB formation, the oldest discovered macro-fossils have been found (El Albani et al., 2010).The overlying shallow-marine massive

dolostones and stromatolitic cherts compose the FC Formation (Bankole et al., 2016) reaching the thickness up to 40 m (Ndongo et al., 2016).

The FD Formation consists dominantly of black shales with fine to medium sandstones interlayering with tuff beds. The depositional setting is interpreted as reducing shallow-marine environment with episodic volcanic material influx (Bankole et al., 2016). The thickness of this unit can be up to 400 m (Reynaud et al., 2018).

Stratigraphically uppermost is the FE formation that is up to 400 m thick (Reynaud et al., 2018) and occurs as a patchy continental piedmont deposit that is mainly composed of coarse and arkosic sandstones with local conglomerate.

Manganese deposition

Manganese is the 10th most abundant element (Kuleshov & Maynard, 2019) and one of the most widely spread transition metals in the Earth's crust (Johnson et al., 2016). Mn-oxides are important scavengers of many elements. The correlation of Co, Ni and Cu with Mn is well-known in the oceanic polymetallic nodules (Gauthier-Lafaye & Weber, 2003).

Manganese has many different oxidation states, but only Mn (II), Mn (III) and Mn (IV) are found in natural conditions. Mn (II) is present in a soluble state and is usually derived from continental weathering and therefore transported fluvially to surface and ground waters. The source of Mn (II) can also be hydrothermal systems at the seafloor (Johnson et al., 2016).

For the formation of manganese-rich sedimentary deposits, the oxidation of Mn (II) to Mn (III, IV) is required (Calvert & Pedersen, 1996). Manganese deposits are classified into four genetic groups: (1) sedimentary and volcanogenic-sedimentary; (2) magmatogenic (hydrothermal and contact-metasomatic); (3) metamorphosed (regional and contact metamorphism of sedimentary and magmatogenic ore accumulations); (4) deposits of the weathering crust (residual, infiltrational). The main part of the global manganese deposits are related to sedimentary basins and are subdivided into sedimentary and volcanogenic-sedimentary deposits by composition and source of manganese (Kuleshov & Maynard, 2019).

The precipitation of manganese in sedimentary environments is mainly controlled by redox and pH conditions. This allows the precipitation of soluble Mn (II) in the form of oxides-hydroxides if oxidised to Mn (III/IV) or in the form of carbonates if remaining in Mn (II) state (Dubois, 2017). The precipitation may be directly related to the oxygen, but can be controlled by the activity of bacteria (Polgári et al., 2012). The first precipitates that concentrate Mn are Mn(IV)oxides. Manganese(III/IV)oxyhydroxides usually form during interaction of deep anoxic and shallow oxic waters (Johnson, 2016) in the shelf environment of stratified basins (Maynard & Force, 1991). This phenomenon can occur during (a) regression, (b) transgression or controlled by upwelling, that brings dissolved Mn (II) from deeper basin to the photic and oxygenated zone or related to down-welling of cold and dense currents that carry dissolved O_2 whereas manganese oxyhydroxides usually precipitate biochemically on detrital nuclei (Maynard & Force, 1991). Precipitation of Mn minerals in sediments has been shown to be strongly controlled by biogeochemical process that promote the Mn (II) oxidation (Polgári et al., 2012) whereas bacterial metallogenesis as part of the formation of Mn deposits has been widely recognized in Mn deposits spanning in age from Precambrian to modern (Fan et al., 1999; Polgári et al., 2012a; Polgari et al., 2012b).

In sedimentary rocks manganese can be also hosted in early diagenetic carbonate minerals (Wittkop et al., 2020) that form in anoxic sediments through diagenetic reduction and dissolution of solid Mn(IV)oxides by organic carbon or at the expense of Mn carried in by hydrothermal fluids which results in the enrichment of Mn (II) in the sedimentary pore water. The reduction processes by organic carbon is usually related to the activity of anaerobic microbes causing the rise of pore water alkalinity that results in Mn (II) precipitation as Mn-bearing carbonates. Paragenetically the first manganese carbonate phases are Ca-rich – kutnohorite and calcian rhodochrosite. Other manganese phases usually form with increasing burial diagenesis and metamorphism (Johnson et al., 2016). Manganese carbonates have characteristically variable content of Mn, Mg, Fe and Ca. These are predominantly represented by different manganese minerals: calcian-rhodochrosite, rhodochrosite, manganocalcite, manganiferous calcite[$MnCO_3$-(Mn_x,Ca_y)CO_3)] and oligonite-manganosiderite-kutnohorite [(Mn_x,Fe_y,Mg_z)CO_3] (Kuleshov & Maynard, 2019).

Precambrian manganese deposits

Manganese rich rocks and ores have formed throughout the geological history of the Earth's lithosphere and are known from the beginning of the Archean but are the most characteristic to Proterozoic and present also in Phanerozoic (Kuleshov & Maynard, 2019). Archean and earliest Proterozoic anoxic oceans had elevated contents of dissolved Mn (II) because of the absence of manganese oxidation before the GOE. Manganese was typically precipitated as carbonate phases, mainly alternating with organic rich shales forming carbonaceous manganese-bearing facies, though large Archean manganese deposits remain unknown (Kuleshov & Maynard, 2019).

The largest Mn deposits were formed prior to or at the onset of the Great Oxidation Event but are common throughout geologic history. In addition, these manganese enrichments reflect fluctuations in Earth's redox balance (Maynard, 2010), ancient oxygen availability and paleo-environmental chemistry (Johnson et al., 2016). The main large manganese deposits formed during Early-Middle Proterozoic epoch of manganese accumulation. Over 80 percent of the world's continental manganese ore deposits are located in Africa. There are four main types of manganese deposits: banded iron formation (BIF)-hosted, black shale-hosted, karst-hosted and oolitic deposits. BIF-hosted deposits in Kalahari Manganese Field, South Africa form 77% of the land-based manganese metal resource. The next largest manganese resource in Africa after Kalahari Manganese Field is the Francevillian Group in Gabon that forms 3% of the world's land-based manganese ore deposits. These are represented by black shale-hosted manganese deposits and are of supergene origin formed after the weathering of Mn-carbonates (Beukes et al., 2016).

The manganese in the Francevillian Group is interpreted to be of volcanic-hydrothermal origin and it is assumed that it reached the edges of the basin due to the fluctuating episodes of transgression-regression and the distribution of Mn-enrichment is controlled by the local paleogeographic situation (Gauthier-Lafaye & Weber, 2003), where the manganese carbonates formed together with an influx of fine siliclastics (Beukes et al., 2016).

Trace elements as proxies of redox conditions

Redox-sensitive trace elements are widely used as paleo-redox proxies for interpretation of redox conditions at the time of deposition or during early diagenesis of ancient sediments and therefore the content of oxygen in the atmosphere and overlying water. Such trace elements that can be used for geochemical proxies are vanadium (V), uranium (U), molybdenum (Mo) and rhenium (Re), and others. Variable solubility and affinity for particulates cause different enrichments of these trace elements in various redox states. Using different values of trace element enrichments it is possible to separate specific depositional environments (Bennett et al., 2020). Redox-sensitive trace metals are soluble and mobile in oxic environment, while less soluble in reducing conditions. Thus, authigenic trace element enrichments occurs in oxygen-depleted facies. Due to the terrigenous detrital inputs, trace metal enrichment values are usually normalized using the division of trace metal (TM) concentrations by aluminium concentrations (TM/Al) (Tribovillard et al., 2006).

Paleo-redox conditions are principally divided into oxidizing or reducing. Anoxic conditions can be whether non-sulphidic or euxinic. Euxinic settings typically occur in semi-enclosed basins, where the hydrogen sulphide is present in the water column. Hydrogen sulphide in euxinic basins is related to the activity of sulphate-reducing bacteria. Anoxic or low-oxygen conditions can develop in sediment-water interface or within sediments, where oxygen demand is higher than supply. Same conditions can occur in stagnant water column, where circulation is marginal for the presence of elevated oxygen level or organic matter degradation is greater than oxygen renewal (Tribovillard et al., 2006).

According to Bennett (2020) the largest V, U, Mo and Re enrichments occur within the seawater column in perennial OMZ *(Oxygen Minimum Zone)*. Under anoxic conditions the trace element enrichments (TM/Al) in perennial OMZ environment are the largest with V > 46 ppm/%, U > 5 ppm/% and Mo > ppm/%. The elevated enrichment values are related to the large flux of reactive solid phases, that can adsorb dissolved elements (particulate organic matter, Fe-Mn-oxyhydroxides) caused by rapid deep-water renewal. Enrichments of Mo (> 5.0 ppm/%) and V (46 - 23 ppm/%) infer to euxinic depositional environment. These, somewhat smaller enrichment values are caused by lower sedimentation rates and water renewal of more restricted euxinic basins. Enrichments of U (> 1 ppm/%), V (< 23 ppm/%) and Mo (< 5 ppm/%) provide evidence for oxic water beneath the core of a perennial OMZ depositional environment. Enrichments of Mo < 0.4 ppm/% Re < 1.3 ppm/% infer to oxic environment (Bennett et al., 2020).

Materials and methods

The samples for this study were taken from the 139 m long LST12 core. Samples were obtained in collaboration with the Comilog-Eramet in Moanda and University of Masuku, Franceville.

LST12 core was drilled in the Lastoursville sub-basin and is covering an interval of Mn-bearing dolostone and black shale of the FB formation (Figure 1). Geological succession in the Lastoursville sub-basin consists of about 200 m thick sandstones of the FA Formation unconformably laying on Archaean crystalline basement. FA is followed by about 100 m thick alternating dolostone and black shale FB succession grading into black shales (Weber, 1968; Azzibrouck, 1983a; Azzibrouck, 1986; Préat et al., 2011). The dolostones in Lastoursville sub-basin are characterized by ^{13}C enriched values ($\delta^{13}C_{carb}$ up to 8.5‰) that decline towards 0‰ in the upper part of the carbonate succession that has been interpreted as correlative to the end of the Lomagundi-Jatuli Event (Préat et al., 2011; Ossa et al., 2018) but recently argued by Bakakas et al. (2020).

For mineralogical and chemical composition, 150 samples were measured. Geochemical data was collected from 33 thin sections, that were made from the core samples between depths of 17 m to 139 m, where Mn content was the highest. Mineral composition and selected elements in whole rock chemical composition (including carbonate C/O isotope data) of the LST12 core sediments were earlier reported in Bakakas et al. (2020).

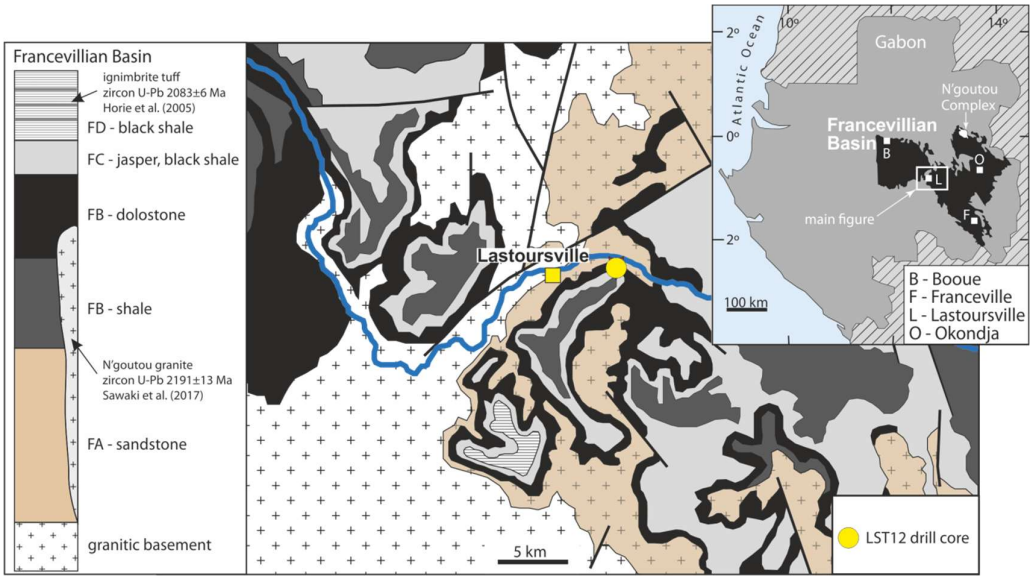

Figure 1. Geological map of Lastoursville basin, showing the location of LST12 drillhole. Compiled by A. Prave and K. Bakakas.

Samples were pulverized in a planetary mill. The mineralogical composition of the LST12 core samples was studied by means of X-ray diffractometry (XRD). Unoriented preparations were measured with Bruker D8 Advance diffractometer with CuKα radiation and LynxEye positive sensitive detector in 2-70° 2-Theta range. The mineralogical composition was modelled and interpreted using the Rietveld algorithm-based program Topaz.

Major and minor elemental composition of pulverised samples dissolved with multi-acid methods (HNO_3, $HClO_4$, HF) were determined by Inductively coupled plasma - optical emission spectrometry (ICP-OES) (Bureau Veritas Minerals, Canada). Average relative standard deviation was less than 5% for all elements.

For micromorphology studies, carbon-coated thin sections were analysed with ZEISS EVO 15MA scanning electron microscope in high vacuum using backscattered electron (BSE) mode. The chemical composition was captured by elemental mapping using Oxford AZTEC-MAX energy-dispersive spectroscopy (EDS) that is attached to SEM.

To eliminate the influence of the detrital component for trace element ratios the trace element concentrations were normalized to aluminium content [($TM_{enrichment}$=Tm (ppm)/Al (wt.%)]. Trace element enrichment factors (EF) in different Units were calculated in respect of crustal average for each metal, where crustal average values are V=11.9 ppm/%, U=0.331 ppm/%, Mo=0.135 ppm/% and median for Re is 0.0365 ppb/% (Rudnick & Gao, 2013).

Results

According to Bakakas et al. (2020) the succession in LST12 core can be divided into six units from Unit I to Unit VI represented by cross-bedded dolostone grainstone and shaly dolomites in Unit I-II, pink-grey in places brecciated dolostone in Unit III, pyritiferous black shale interlayered with ca. 10 cm-thick beds of massive dark-grey to black dolostone in Unit IV, light- to dark-grey dolo-rhythmite interbedded with laminated dolostone in Unit V and Unit VI is represented by black shale with thin beds of laminated to massive carbonate beds (Figure 2). Sedimentological interpretation of the succession suggest tidally influenced shallow-marine environment during deposition of Units I-III whereas brecciated dolostone in Unit III indicates palaeokarst features (Bakakas et al., 2020; Préat et al., 2011). Units IV to VI represent deepening of the basin below the storm-wave base (Bakakas et al., 2020).

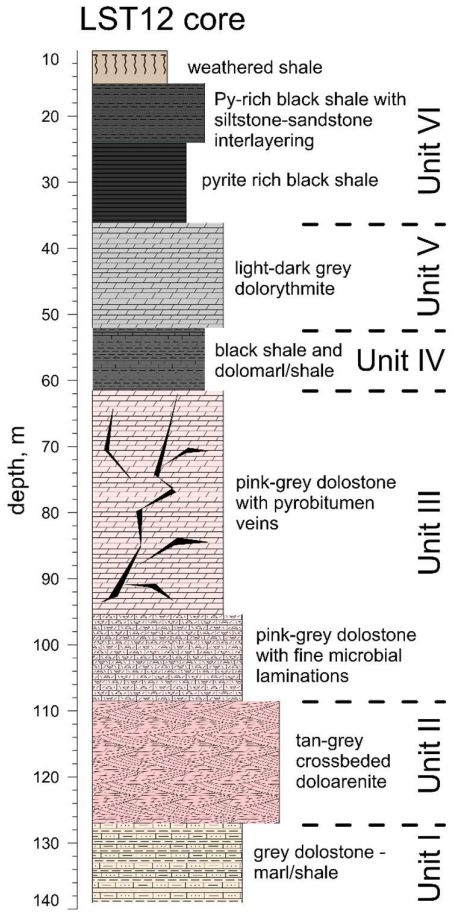

Figure 2. Lithology of the carbonate-shale succession in LST12 core. Modified after Bakakas et al. (2020).

Carbonate petrography

Petrography and microstructure of carbonate phases and distribution of major elements were observed using scanning electron microscope (SEM) in back-scattered electron (BSE) mode. In back-scattered electron image minerals with higher average atomic number (pyrite, apatite, calcite) appear as lighter areas, while materials with low average atomic number (quartz, dolomite, carbon) show up darker. SEM with energy dispersive spectroscopy (EDS) was used for elemental distribution mapping. The presence of Ca with carbon typically represents calcite, while with P it refers to the presence of Ca-phosphate. Co-occurrence of Mg and Ca with carbon is an indicator of dolomite, whereas additional Fe and Mn can indicate the presence of ankerite or kutnohorite-type carbonates. Fe and Mn composition with carbon indicates siderite and rhodochrosite, respectively.

Carbonate minerals in Unit I are mainly characterized by tightly packed dolomite crystals (Figure 3 a, b) with variable size, shape and abundant calcite replacement and/or overgrowths, probably caused by dedolomitization. This is indicated by BSE images of brighter spots or patches, where Ca content is higher (3 c). Dolomite crystals can be rhombohedral with more ankerite-type rims, caused by Fe substitution (Figure 3 d) or anhedral as tightly packed (Figure 3 e, f). Occasionally few zoned carbonate crystals occur, where more Fe-rich carbonate is rimmed with dolomite. The pore space between carbonate crystals is mostly filled with quartz, mica (+chlorite), K-feldspar and plagioclase. In addition, zircon, rutile, fluorapatite and pyrite is present.

Unit II is characterized by shale interbeds (Figure 4 a, b) that are marked by K-feldspars, plagioclase and micas with few chalcopyrite, pyrite and rutile grains. Within the shales, occasional rhombohedral dolomite crystals occur that are rimmed with ankerite-type carbonate and have abundant inclusions and growth zones (Figure 4 c, d).

Carbonate phases in Unit III are represented by massive, tightly packed dolomite crystals (Figure 5 a) with occasional weak zonality, where the rim of dolomite core has a small Mn and Fe addition. Overall, it is difficult to identify the shape of individual crystals. However, in some cases, clear rhombohedral shapes are recognizable (Figure 5 g). According to BSE images and EDS analysis, slightly lighter and darker areas or brighter spots in dolomite crystals indicate patches of variable Ca-Mg ratios and abundant replacements by calcite (Figure 5 c, d, e, f). Slightly higher Fe content shows the presence of rare ankerite-type carbonate phase. Also, there abundant calcite overgrowths and pyrobitumen veins (Figure 5 b, h). Fractures in brecciated

dolostone are filled with calcite and silica. Overall, in the interstices between dolomite crystals, silicate minerals with apatite crystals or crystal-aggregates and pyrite occur (Figure 5 c, d, g).

Unit IV is characterized by interlayering of shales and dolostones. Organic-rich shales are mainly composed of K-feldspar, plagioclase, micas and quartz with additional zonal pyrite aggregates, apatite and TiO_2 mineral. Occasional carbonate crystals are of dolomite or ankerite composition with variable morphology. Dolostones are composed of tightly packed rhombohedral dolomite crystals (Figure 6 a, b) of varying composition. Typically, zonal dolomite crystals have dolomite core and minor addition of Fe and Mn on the edges, that is indicated by slightly lighter outer zone in BSE images (Figure 6 d). These are often in contact with dolomites with abundant bright spots, indicated as calcite by EDS analysis (Figure 6 d). Some dolomite crystals can have two consecutive Fe-Mn-rich rims, whereas the inner zone has higher Fe-Mn contents (Figure 6 g, h). In some cases, zoned dolomites have ankerite-type core and rim (Figure 6 c), while few purely Fe-rich ankerite-type carbonate crystallites are also present, but these can represent the cross-sections of the larger rimmed dolomite crystals cut through the outer parts of the crystallite in thin-section plane. In addition, some massive dolomites have minor Mn content that is increasing towards the edge and is recognizable with a bright rim (Figure 6 e, f). Pore space is mostly filled with quartz and K-feldspar. There are also apatite crystals and aggregates, framboidal pyrite, pyrite and TiO_2 mineral.

Unit V is characterized by tightly packed anhedral or rhombohedral dolomite crystals (Figure 7 a). In most cases, rhombohedral dolomite crystals have two consecutive Fe-Mn-rich ankerite-type rims, inner Fe-Mn rich zone and the outer zone with slightly lower Fe-Mn content. This is exemplified by the bright rim around the dark dolomite core and the slightly darker outer rim in BSE images (Figure 7 e, f). In addition, kutnohorite overgrowths/inclusions or aggregates are present with elevated Ca and Mn content (Figure 7 b). In some cases, it appears that anhedral dolomite crystals with minor Fe and Mn content have abundant calcite and dolomite inclusions/overgrowths. This is indicated by lighter and darker areas/patches in BSE images (Figure 7 c). EDS images show high Ca concentrations in brighter spots and Ca together with Mg in darker areas (Figure 7 d). Slightly lighter areas indicate elevated Fe and Mn content. The interstices between carbonate crystals are filled with plagioclase, quartz, rutile and pyrite.

Unit VI is composed of organic-rich shales that contain abundant quartz, K-feldspars, plagioclase, micas and pyrite (Figure 8 a, b, c, d). Several types of carbonates can be recognized. Occasionally, rare rhombohedral inclusion-rich ankerite crystals occur, while some of these have dolomitic core. More abundant are anhedral and rhombohedral carbonate crystals with

variable size. Anhedral, patchy carbonates are siderite-type with Mn-rich areas and abundant quartz, plagioclase or K-feldspar inclusions, however, some siderite carbonates can be rhombohedral. Occasionally, Mn-rich siderites occur (Figure 8 j). Rhombohedral, zoned, mainly kutnohorite-type carbonate crystals-aggregates are present in sediments as lens-like layers, that is surrounded by pyrite aggregates. According to EDS analysis and darker areas in BSE images, the core and rim appear to be more of Mn-rich ankerite-type carbonate (Figure 8 e, f, g). Frequently rhombohedral ankerite crystals with Mn-rich kutnohorite core occur (Figure 8 m). Occasionally concentric/round kutnohorite-type carbonates with ankerite rim appear as individual crystals or as lens-like layers (Figure 8 h, i, k, l). The space between kutnohorite crystals is filled with quartz, K-feldspar and micas. Also, pyrite interlayers with different pyrite morphology occur, where rounded isometric pyrites are abundant. The upper part is covered with inclusion-rich pyrites, possibly after volcanic glass. The occurrence of framboidal, sometimes zonal (Figure 8 n) pyrite aggregates with typical sizes of 15-30 μm and bending of mudstone layers provide evidence for early diagenetic formation of such aggregates. Carbonate rich lens-like layers in Unit VI are interlayered with microbial like textures, fine, organic-rich microlaminae with thin “crinkly” bedding (Figure 8 a, d).

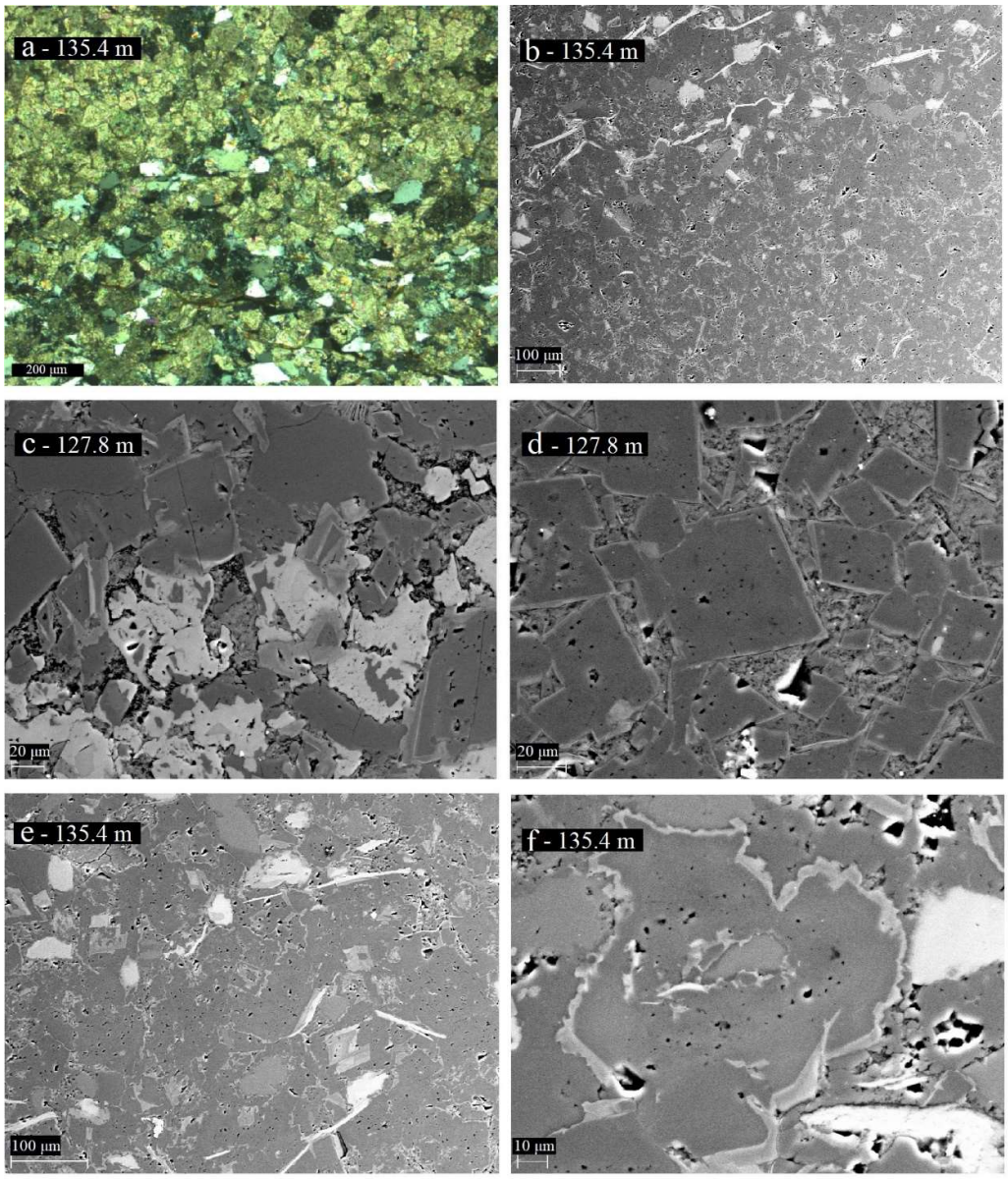

Figure 3. SEM BSE images of Unit I: (a) optical microscope image of dolomite crystal aggregate in the upper part of the image and higher additional mica, quartz and feldspars in the lower part; (b) massive dolostone with mica, quartz and feldspars in the upper part; (c) tightly packed dolomite crystals with calcite replacement/overgrowths; (d) rhombohedral dolomite crystals with Fe-rich rim; (e) massive dolostone with feldspars, quartz and mica; (f) anhedral dolomite crystal with ankerite-type rim and plagioclase inclusion.

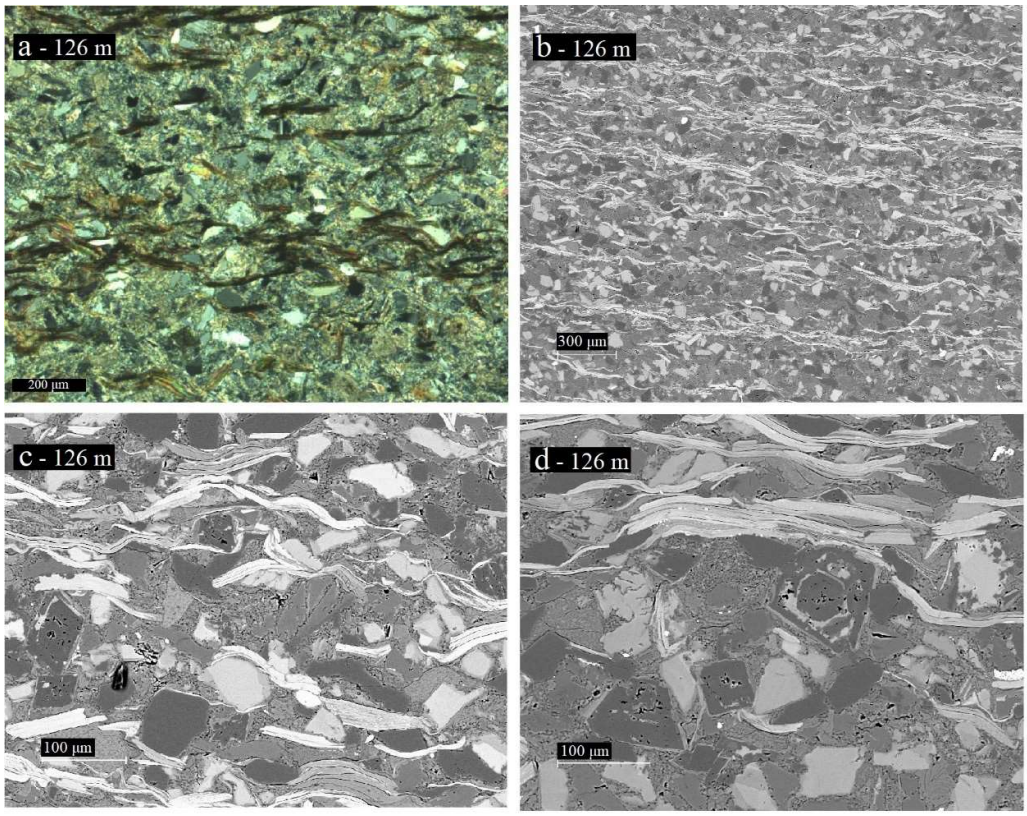

Figure 4. SEM BSE and optical microscope images of Unit II: (a) optical microscope image of mica-quartz-feldspar shale interbed with dolomite; (b) BSE image of the mica interbeds in unit I carbonates; (c, d) rhombohedral dolomite crystals with Fe-rich rim, micas, K-feldspar, plagioclase, quartz. Note several growth zones in the dolomite crystal in the centre of image d.

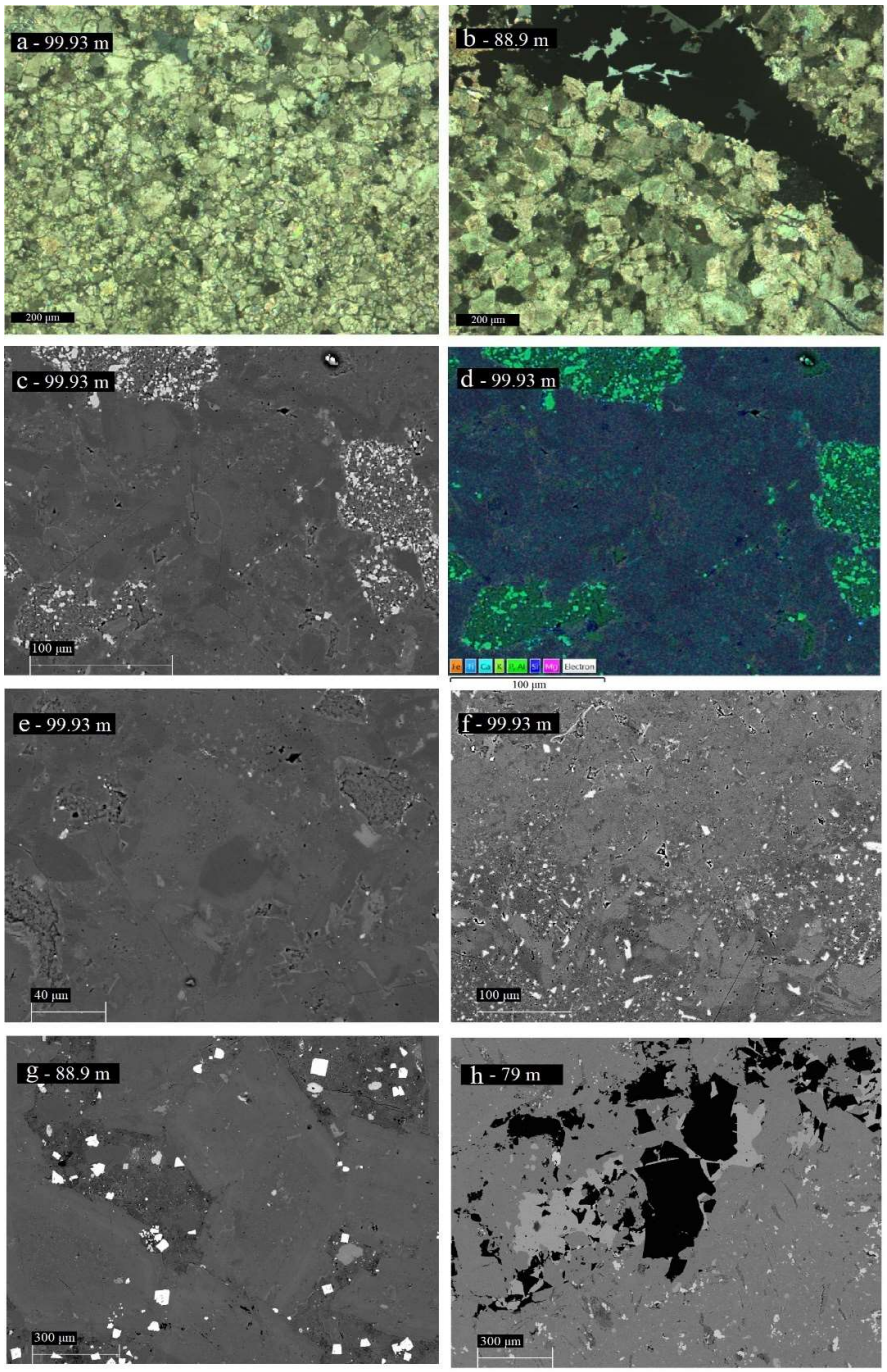

Figure 5. SEM BSE, EDS and optical microscope images of massive dolomite of Unit III (a) optical microscope image of massive dolostone; (b) optical microscope image of pyrobitumen vein in brecciated dolostone; (c, e, f) dolomites with variable ratio of Ca-Mg; (d) overlay image of chosen elements; (g) rhombohedral dolomite crystals with weak zones, silicate composition pore filling with scattered pyrite cubes; (h) tightly packed dolomite crystals with calcite overgrowths and fractured pyrobitumen pore fillings/veins (black areas on image).

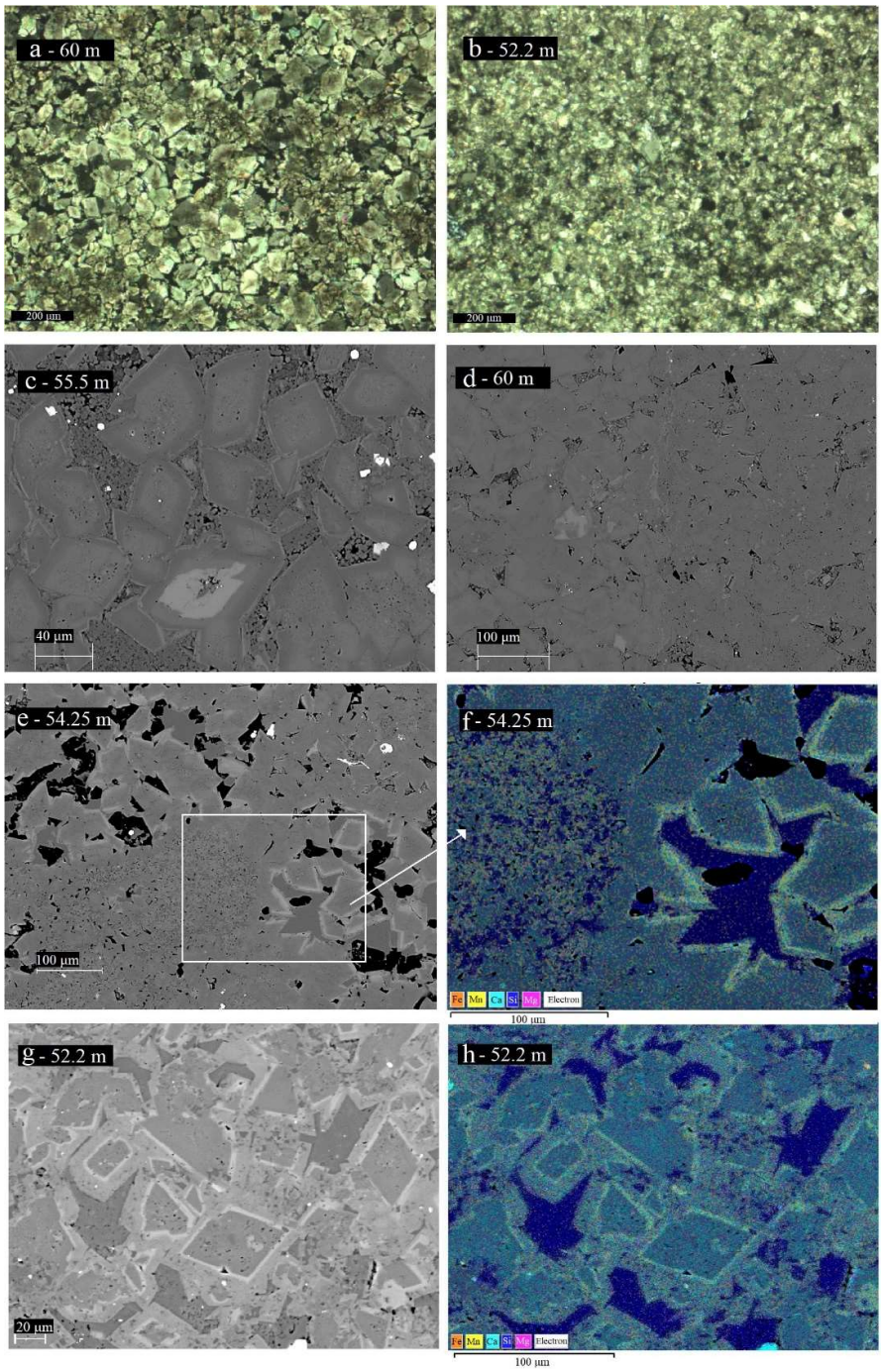

Figure 6. SEM BSE, EDS and optical microscope images of Unit IV (a, b) optical microscope images of massive dolomite of different crystal size ; (c) zonal dolomites with ankerite core and rim; (d) dolomites with weak zonality and/or calcite overgrowths; (e) tightly packed dolomite crystals with Mn-rich rim and quartz pore space filling; (f) overlay image of chosen elements; (g) dolomite crystals with dolomite core and Fe-Mn-rich outer zones; (h) overlay image of chosen elements.

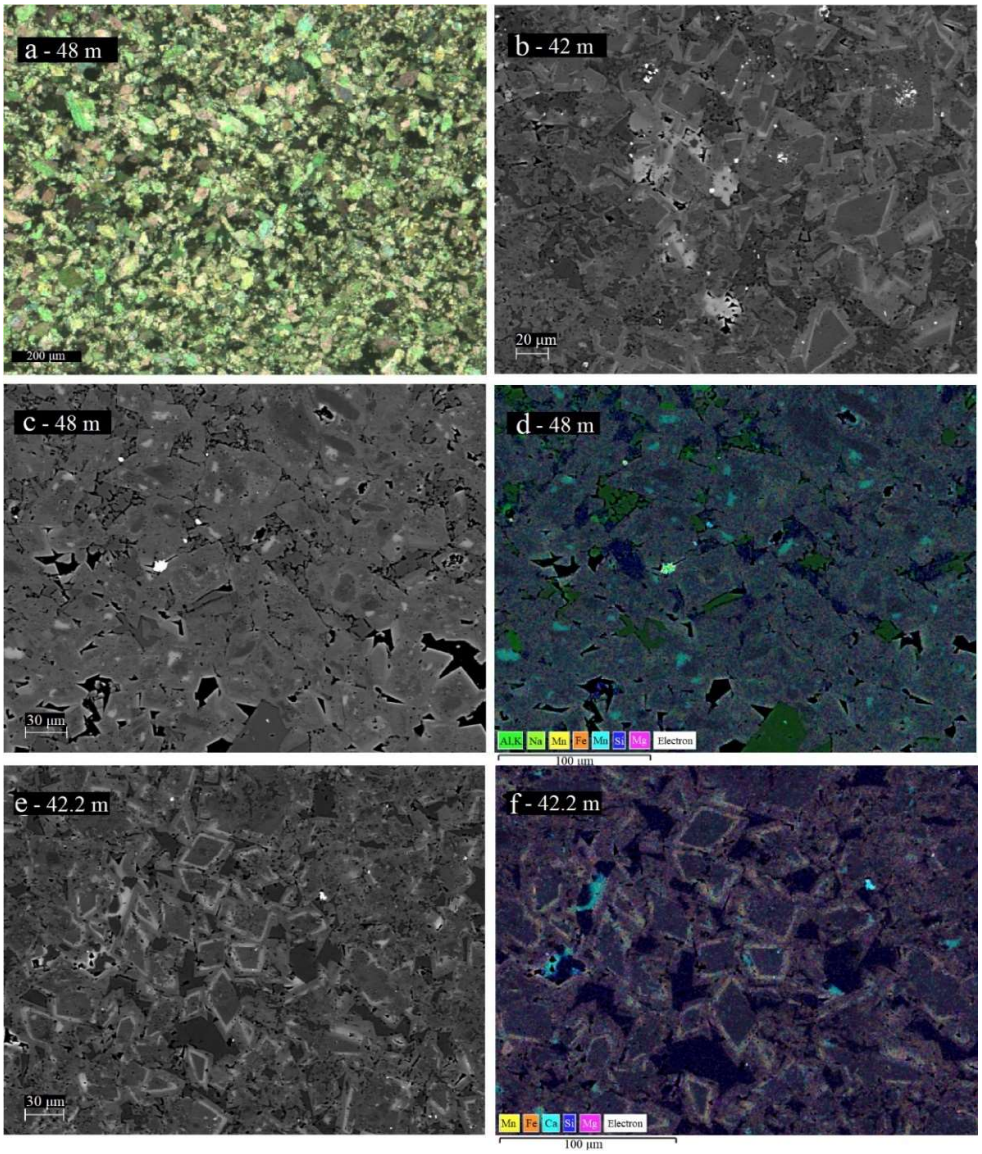

Figure 7. SEM BSE, EDS and optical microscope images of Unit V (a) optical microscope image of anhedral carbonate crystal aggregate; (b) kutnohorite inclusions/aggregates in rimmed dolomite crystals; (c) anhedral dolomite crystals with abundant calcite and dolomite overgrowths; (d) overlay image of chosen elements; (e) dolomite crystals with two Fe-Mn-rich ankerite rims; (f) overlay image of chosen elements.

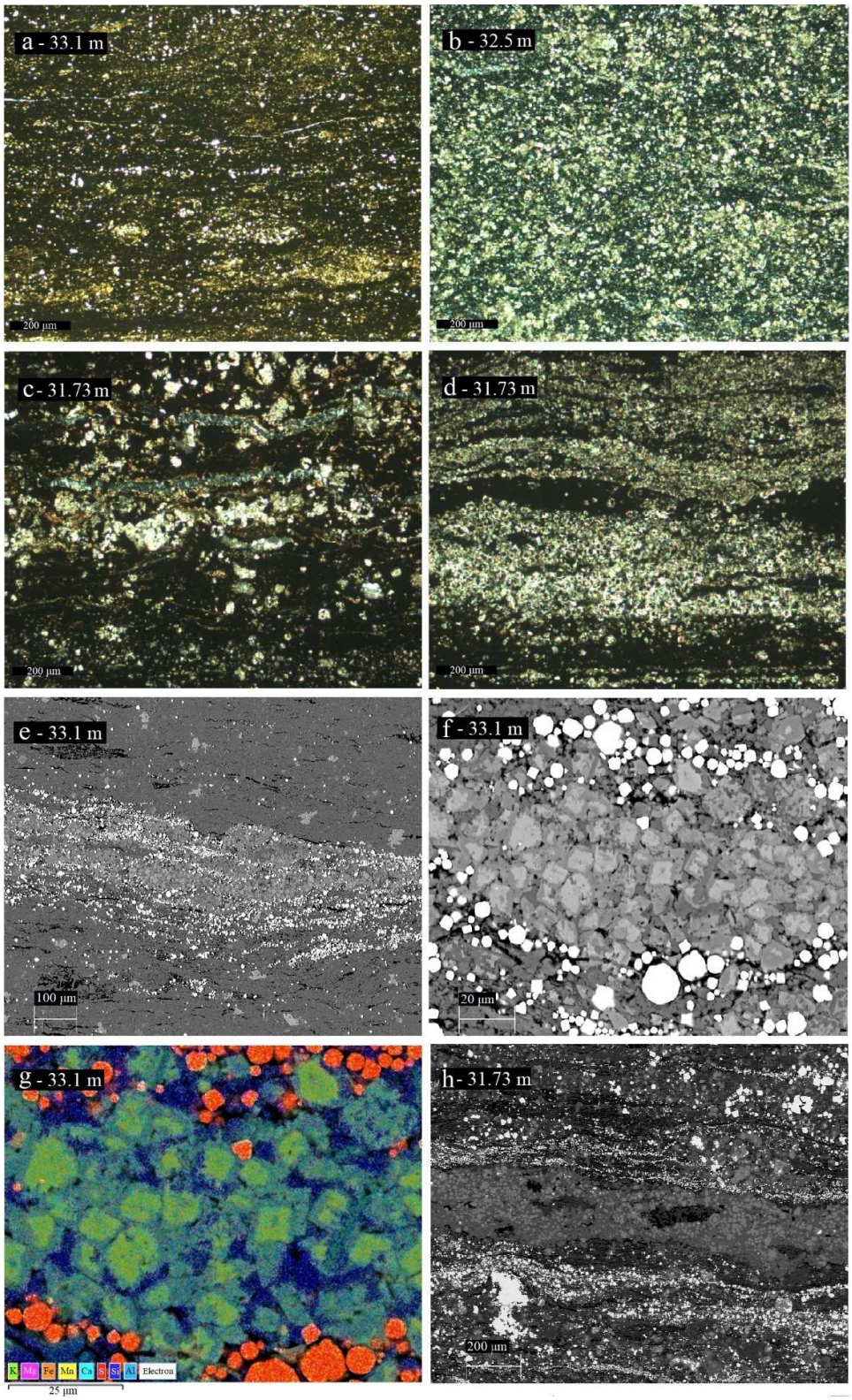
a - 33.1 m
200 µm
b - 32.5 m
200 µm
c - 31.73 m
200 µm
d - 31.73 m
200 µm
e - 33.1 m
100 µm
f - 33.1 m
20 µm
g - 33.1 m
K Mg Fe Mn Ca S Si Al Electron
25 µm
h - 31.73 m
200 µm

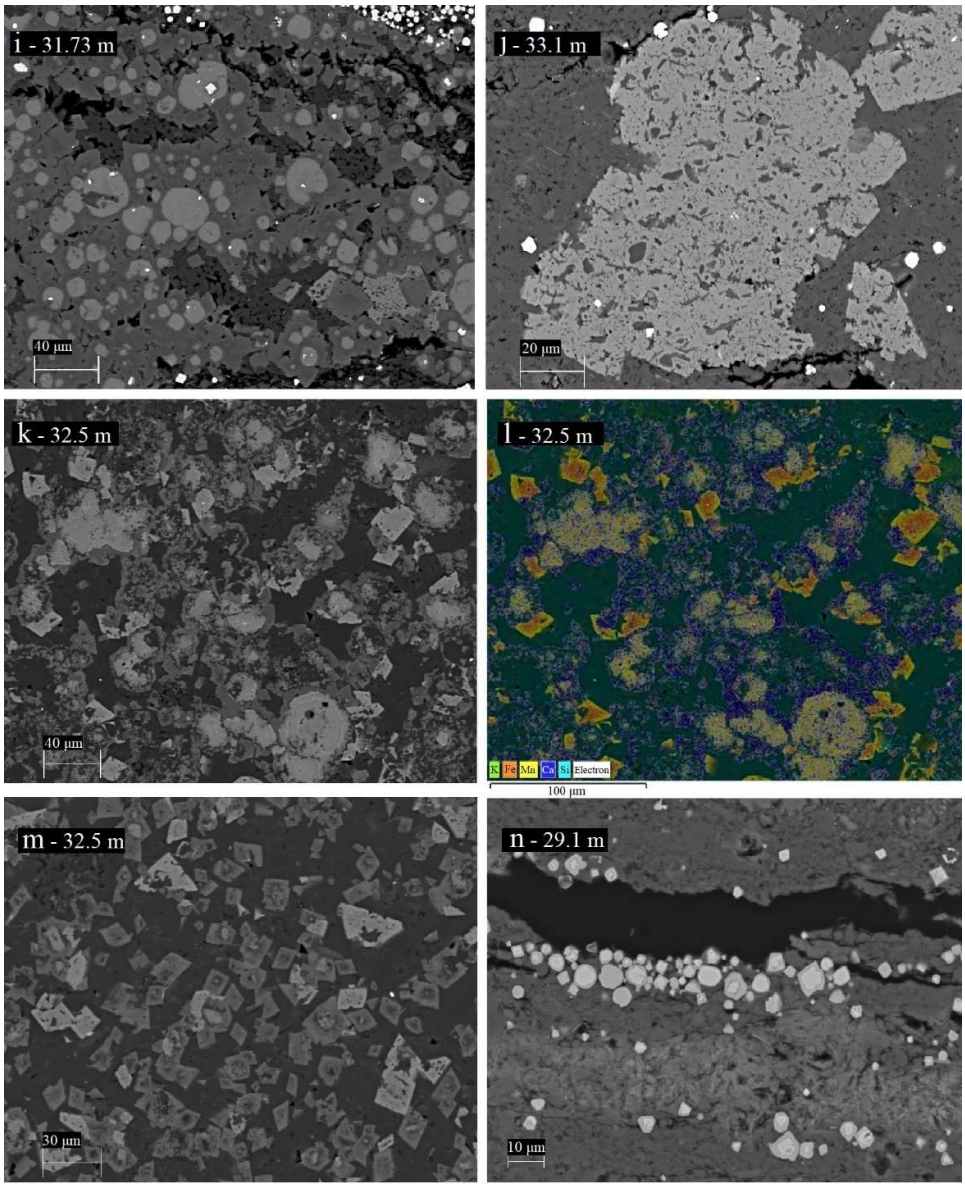

Figure 8. SEM BSE, EDS and optical microscope images of Unit VI: (a, b, c, d) optical microscope images of lens-like carbonate layers in organic-rich shale, possibly indicating microbial lamination (Polgári et al., 2012); (e) lens of rhombohedral kutnohorite carbonate crystals in shale; (f) rhombohedral zoned kutnohorite carbonate crystals with ankerite core and rim, surrounded with pyrite disseminated crystals and framboidal aggregates; (g) overlay image of chosen elements; (h) lens of kutnohorite and ankerite carbonates in organic-rich shale; (i) round kutnohorite carbonates crystals/-aggregates surrounded by Mn-rich ankerite; (j) Mn-rich siderite crystal with abundant inclusions; (k) siderite carbonates; ankerite crystals with occasional dolomite core; concentric kutnohorite carbonates with ankerite rim; (l) overlay image of chosen elements; (m) rhombohedral ankerite crystals with Mn-rich kutnohorite core; siderites; (n) framboidal zonal pyrites in organic-rich shale.

Whole rock mineralogy and chemistry

Whole rock mineral and chemical composition of sediments in LST12 core are reported in Bakakas et al. (2020) and shown in Figure 9 and Figure 10. By mineral composition, Units I and II are dominated by mixed quartz-feldspar-mica-carbonate mineral assemblage with dolomite varying from few percent in shale interlayers to nearly 90% in the carbonate bed. More shale-siltstone rich interbeds in Units I and II are composed of phyllosilicate mica, mainly K-mica which content varies between 20–40%, that is characterized by high concentrations of K, Al and Na (Figure 10). In lower units also K-feldspar and plagioclase make up to 20–30% whereas quartz is rather stable at 20% of the mineral composition. Content of terrigenous mineral degrades gradually through the Unit I to Unit II as it is typically less than 10% in the upper part of Unit II and in Unit III. The dolomite content increases upwards in Unit II from about 50–60% to 85–95% and stays at about 60–80% of the mineral phases in Unit III with high level of Ca and Mg relative to K, Al and Na (Figure 10). In brecciated parts of Unit III, the calcite content can rise to about 20% but is generally less than 5–6%. Apatite is present in Unit III and varies from trace amounts up to around 4% of the mineral composition. Composition of Unit IV is characterized by interlayering of shales and carbonates as seen by the content alternation of Ca-Mg and K-Al in Figure 10. Shales/siltstones are mainly composed of mica-quartz-feldspar assemblage. Carbonate beds are characterized by dolomite with 70–90% of the mineral composition, whereas in shales, concentrations increase upwards from few percent up to 30%. Carbonate interlayers include minor occurrence of calcite, typically less than 1%, but rising to 5% in the upper part of the Unit. Compared to Unit I, II and III, pyrite is more abundant and is concentrated in shale interlayers with the highest elevation of 16%. Together with K-mica, shales are mainly dominated by K-feldspar that have the highest contents in the lower part of the Unit IV and decreasing towards the upper part. In shales, K-feldspar content is mainly in the interval of 10–20%, but occasionally reaching up to 40%, whereas in carbonate interlayers, K-feldspar content remains mostly around 1%. K-mica content varies between 20–35% in shale intervals and is less than 1% in carbonate beds, occasionally reaching up to 2–4%. In shales, quartz varies between 30–40%, but have elevated content in the lower part of the unit with 60–80%, whereas in carbonate interlayers, the quartz is a minor phase with 2–5% in the lower part, yet 10–20% in the middle and upper zone. By mineral composition Unit V is dominated by dolomite that is decreasing towards the upper part from 70–80% to 50–60%, while quartz represents the opposite trend by increasing upwards from around 15–20% to 30–40%. The content of K-mica remains less than 1% in most cases but is up to 5–12% in the upper part of the unit. Concentration of K-feldspar stays stable around

1–2% of the mineral composition. The content of calcite increases already in the upper part of the Unit IV reaching 5% and varies between 2–5% throughout the Unit V with slightly lower values in the upper part. Pyrite was found in trace amounts (< 0.5 wt.%). Unit VI is dominated by mica-quartz-feldspar assemblage, where K-mica varies mainly between 20–40%. Quartz shows values at 40–50%, reaching occasionally up to 70% of the mineral composition. Plagioclase content can rise to 10% but is mainly stable at 4–6%. Ca and Mg contents are small (Figure 10) with dolomite mostly less than 2% of the mineral composition. However, in some samples dolomite content around 10%. Calcite proportion is minor with less than 1%. Siderite is identified only in Unit VI with variable content that can rise up to 6% but mainly remains less than 1%. In Unit VI, apatite was found only in two samples with 1.7% and high concentration of 25%. Unit VI shales are pyrite-rich with 4–5% of the mineral composition in the lower part of the Unit and decreasing towards the upper part by remaining less than 1%, yet occasionally can rise up to 12% (Figure 9; Figure 10).

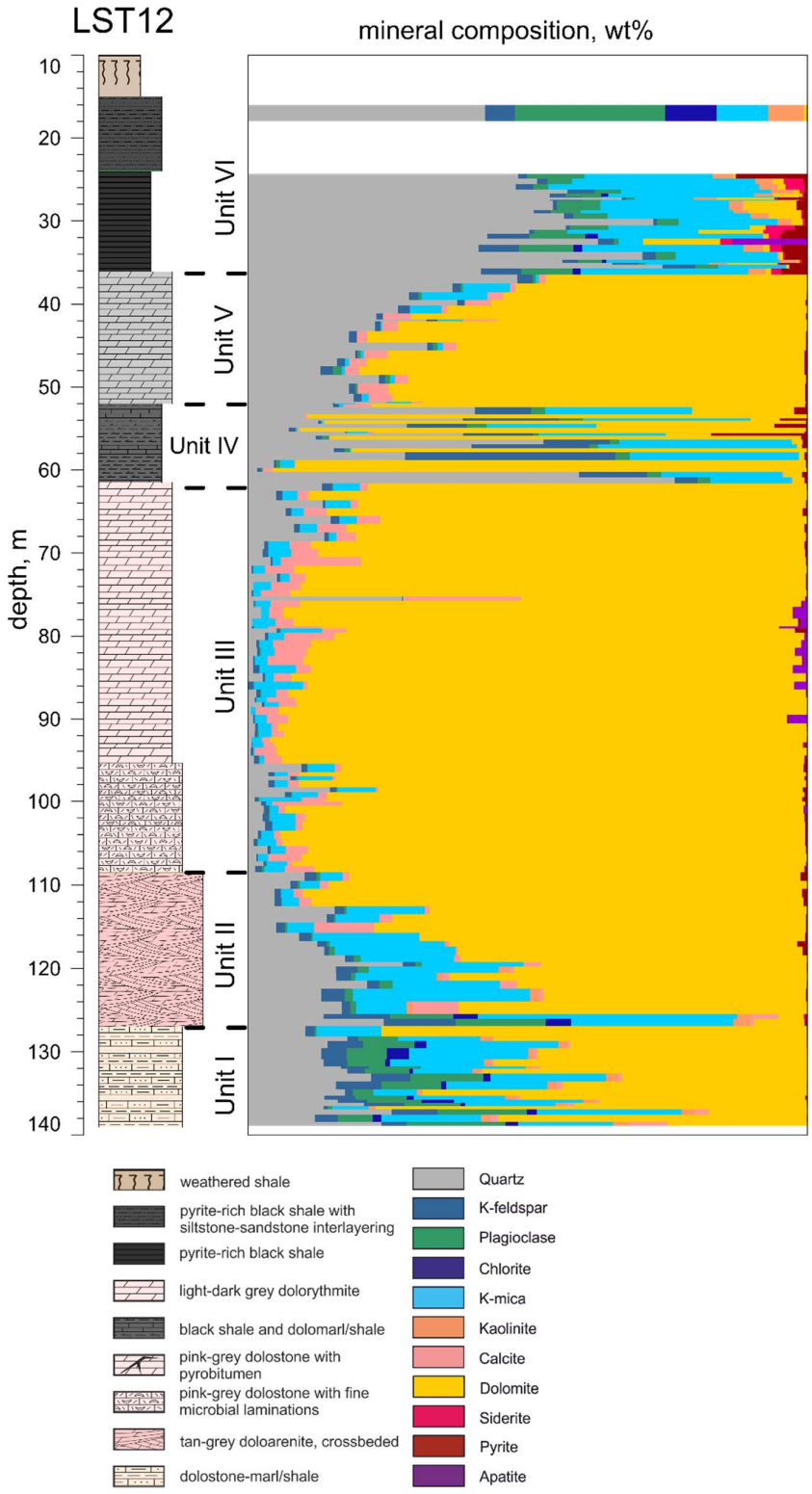

Figure 9. Lithostratigraphic column and mineralogy of the studied samples.

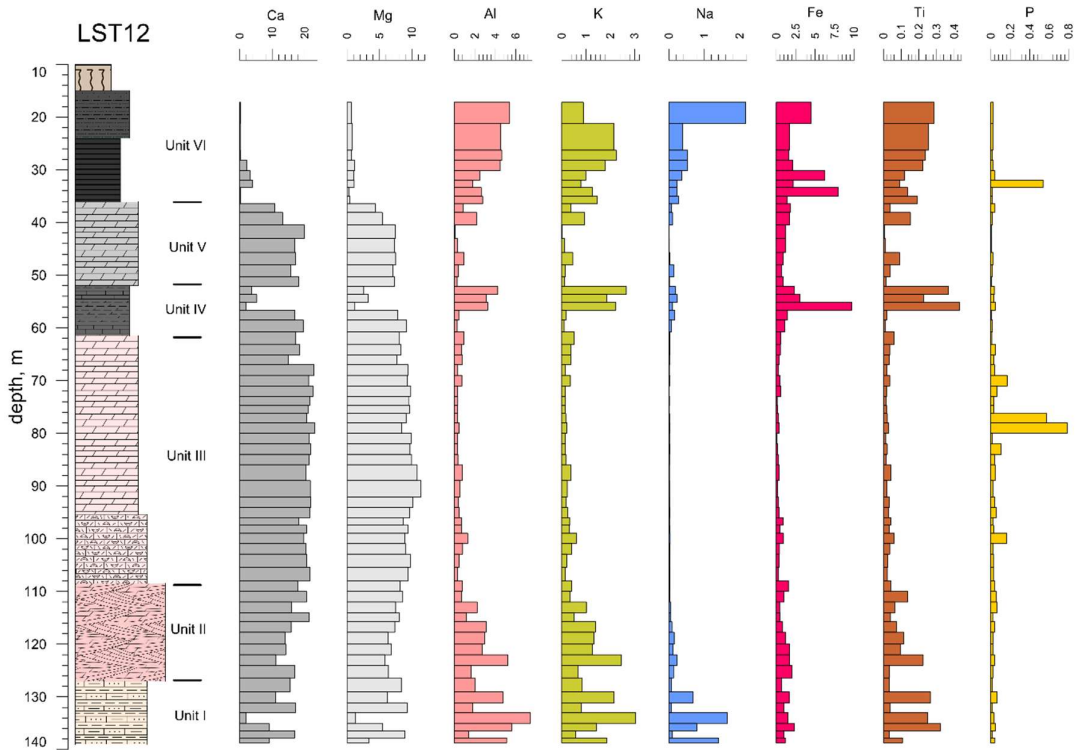

Figure 10. Lithostratigraphic column and chemical composition of the studied samples. See the lithostratigraphic legend in Figure 9.

Chemical composition of the whole rock samples corresponds to the changes in mineral composition with variations of Ca and Mg directly reflecting the abundance of carbonate minerals over the terrigenous phase. Abundance of manganese in LST12 core increases abruptly in Unit V dolo-rhythmites and lower part of the Unit VI pyrite-rich black shales, where Mn concentrations are exceeding 1000 ppm. The largest measured concentrations are in the lower part of the Unit VI shales with the highest of 14260 ppm. In Units I-III manganese concentrations are lower than 1000 ppm, with the lowest abundance in Unit I (Figure 11). Mn/Ca ratio in LST12 core is reflecting Mn substitution in carbonate minerals to Ca and shows a gradual increase already from upper part of the Unit III at 80 m depth and exhibits the highest ratio in Units IV-VI. This indicates an appearance of Mn-enrichment already in carbonates from Unit III upwards, where the main carbonate phase is still dolomite. Mn concentrations, Fe/Al and Mn/Al ratios are abruptly higher in Unit V compared to other Units. At the same time S and Fe show low contents in Unit V and are more concentrated in pyrite-rich Units IV and VI.

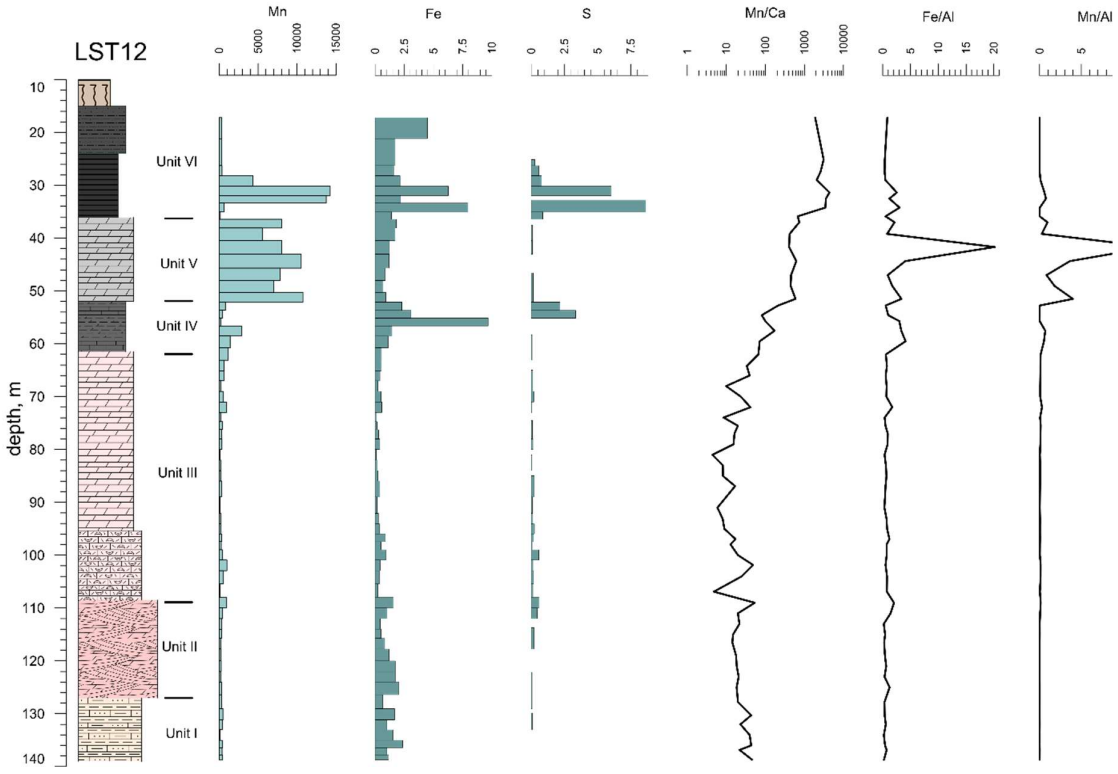

Figure 11. Manganese, iron and sulphur concentration and Mn/Ca, Fe/Al and Mn/Al ratio variations in LST12 core with respect to depth. See lithostratigraphic legend in Figure 9.

Carbonate mineral chemistry

Carbonate minerals in LST12 succession, particularly the carbonate phases in Mn-rich black shales show large compositional variability. Data for the composition of carbonate minerals was collected with *in-situ* point analysis using SEM-EDS. Ternary plot (Fe+Mn)-Ca-Mg (Figure 12) shows variation of carbonate cation chemistry from calcite to dolomite and to ankerite. Units I-V are mainly composed of dolomite with occasional calcite and are typically characterized by low content of Fe and Mn, mainly measured from outer parts of larger zoned dolomite crystals. Also, carbonate minerals in Unit V are represented by nearly stoichiometric dolomites but in some cases, Fe and Mn concentrations are higher and carbonate composition approaches close to ankerite. In contrast, increasing contents of Fe and Mn in carbonate phases in Unit VI indicate dominant presence of more ankerite-type and Mg-rich Fe-Mn carbonates. Ternary diagram of Fe-Ca-Mg (Figure 13) carbonate chemistry shows mostly the presence of dolomite in Units I-V with some calcite occurrence and occasionally higher content of Fe. In Unit VI, carbonates vary from ferrous dolomite and calcite to Mg-rich siderite. Ternary plot in Figure 14 represents carbonate composition changes with respect to Mn-Ca-Mg that also point

to mainly dolomite composition in Units I-V. Mn is absent (or below the detection limit of EDS method, <0.1%) on only minor cations in carbonate phases in Units I-IV, but its content slightly starts to increase in dolomites in Units IV and V. In some cases, Mn-rich carbonates are close to kutnohorite composition already in Unit V. In Unit VI, carbonate phases vary in respect of Mn content from Mn-rich dolomite to kutnohorite to Mg-rich Mn-carbonates. By composition the Mn-carbonate minerals in LST12 succession are thus represented by calcian-rhodochrosite, possibly also manganiferous calcite [$MnCO_3$-(Mn_x,Ca_y)CO_3)] and additionally phases of oligonite-manganosiderite-kutnohorite [(Mn_x,Fe_y,Mg_z)CO_3] solid-solution series.

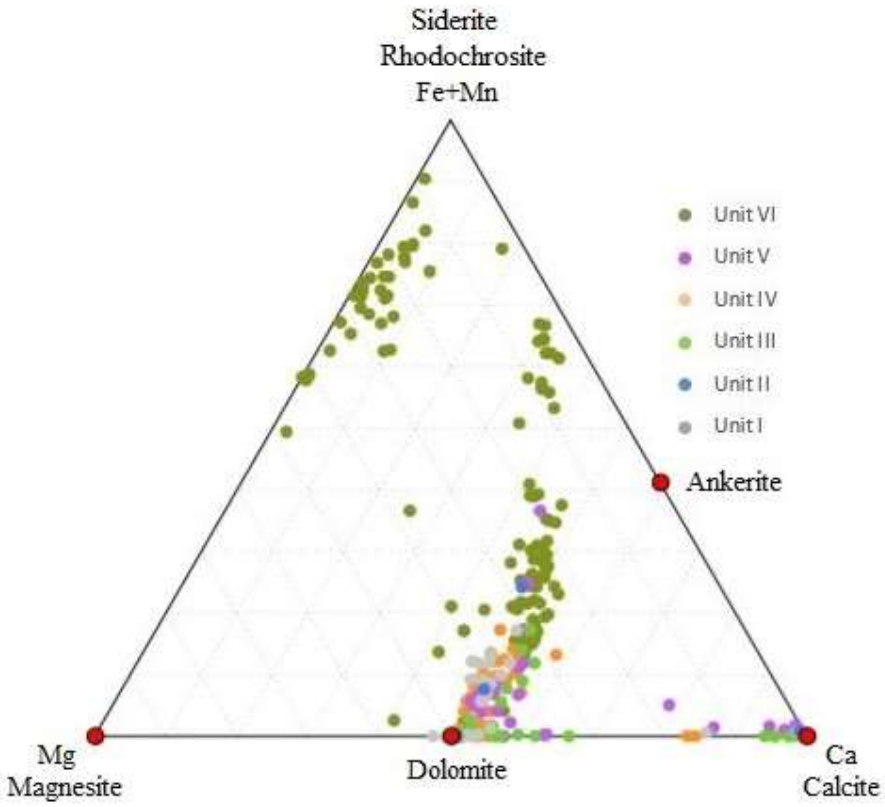

Figure 12. Ternary plot of the carbonate mineral composition in Units I-VI in (Fe+Mn)-Ca-Mg system.

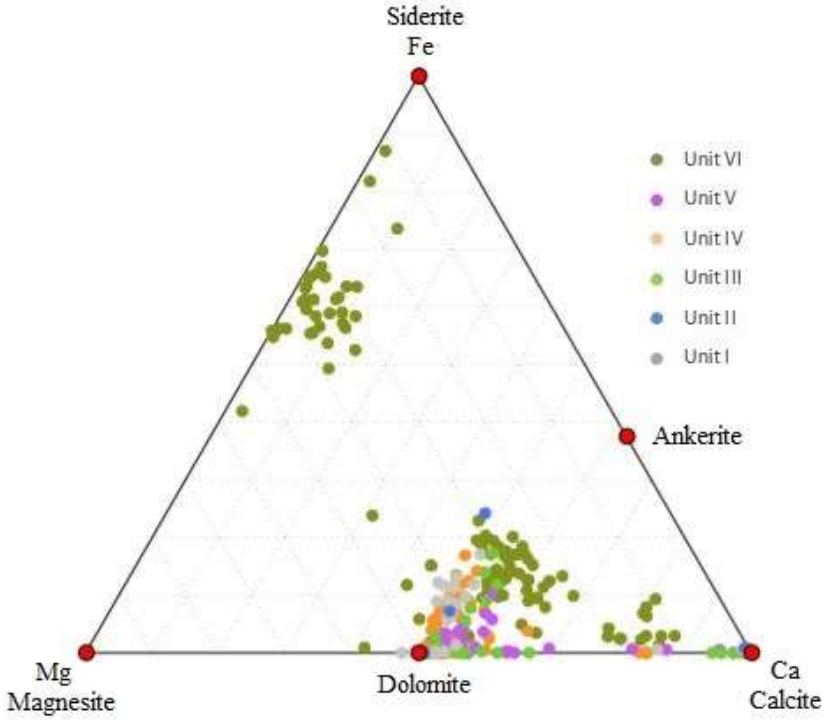

Figure 13. Ternary plot of the carbonate mineral composition in Units I-VI in Fe-Ca-Mg system.

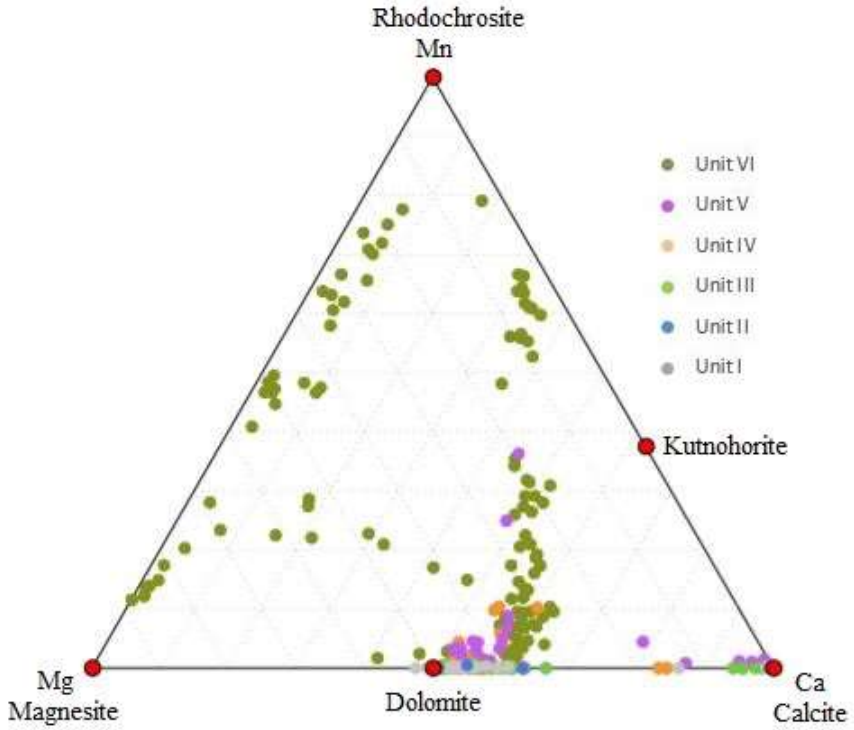

Figure 14. Ternary plot of the carbonate mineral composition in Units I-VI in Mn-Ca-Mg system.

Total organic carbon (TOC)

Total organic carbon concentrations are mainly <1 % in Units I, II, III and V (Figure 15). Significantly higher TOC contents occur in shale intervals of Unit IV and VI reaching up to 14.1%. Overall, the median TOC content in shales of Unit IV is approximately 6.1 wt.%, while 4.2 wt.% in Unit VI shales.

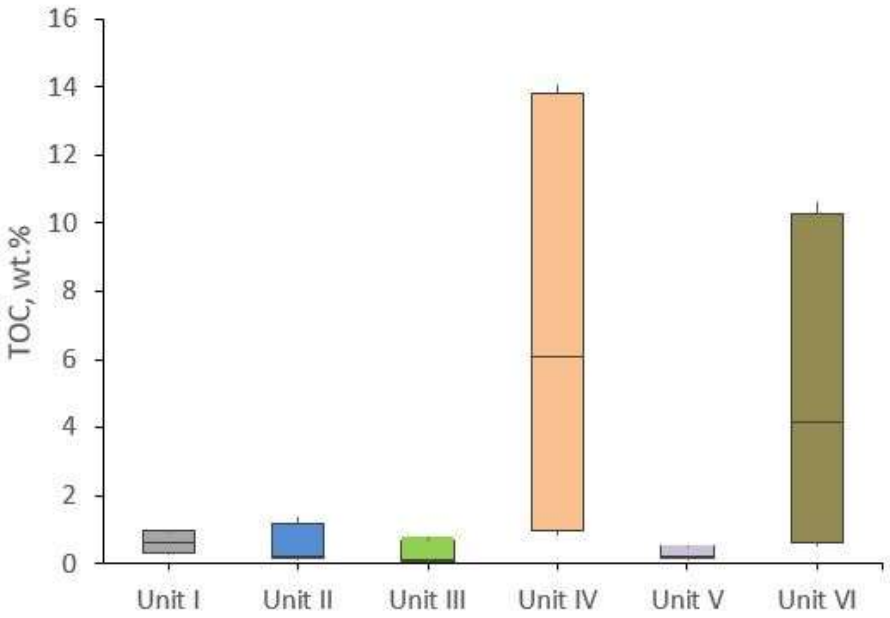

Figure 15. Total organic carbon (TOC) concentrations in different Units of the LST12 core. TOC concentrations are plotted as box and whisker plots in interquartile range, where the whiskers represent the 5th and 95th percentiles for TOC concentrations. The mean of each unit is shown as a stripe.

Discussion

Carbonate mineral precipitation and diagenetic Fe-Mn enrichment

Distribution of Mn (and Fe) in carbonate minerals of the LST12 core shows a distinct change from carbonate mineral diagenetic enrichment with respect to Mn and Fe and formation of zoned overgrowths on primary dolomite precursor in lower part of the carbonate bearing succession (Units I-III) to Mn/Fe-enriched primary dolomitic carbonate phase in Units IV and V, and complex Mn,Ca,Fe,Mg-carbonate minerals in the uppermost shales of Unit VI. This transition possibly reflects changing redox and diagenetic conditions during the deposition of the LST12 succession.

In Units I, II and III the composition of the dominant carbonate phase is close to a stoichiometric dolomite in the centre of the dolomite rhombohedral crystals. The outer rims of the dolomite show slight enrichment in Fe and to some extent in Mn. The overall composition shows a trend towards ankerite type carbonates (see Figures 12, 13) indicating late diagenetic recrystallization and Fe/Mn uptake.

Fe^{2+} and Mn^{2+} (and Sr^{2+}) are typical minor elements in diagenetic dolomites (Swart, 2015) potentially replacing both Ca^{2+} and Mg^{2+} in dolomite structure (Vahrenkamp & Swart, 1994) whereas Mn is preferentially replaced to the Mg sites. Precipitation of pore filling diagenetic dolomite or formation of Fe-Mn enriched overgrowths on stoichiometric dolomite nucleuses is controlled by the pore fluid composition suggesting that the porewater was saturated with Fe(Mn)-dolomite. Increase in dissolved Fe^{2+} and Mn^{2+} in pore fluid in lower carbonate dominated Units was most possibly driven by organic matter (microbial) reduction in sediments leading to reductive dissolution of detrital Fe- and Mn-(oxy)hydroxides but also elevated alkalinity supporting the precipitation of Fe/Mn rich dolomite rims (Petrash et al., 2016; 2015).

In Units IV and V, however, the diagenetic overgrowth zones are well-defined and wider compared with dolomites in Unit I-III suggesting precipitation in environment with high carbonate saturation and Fe-Mn-enriched fluid. Though the carbonate precipitation was still driven by dolomite nucleation, the porewater conditions rapidly changed. For that reason, in Units IV and V, the formation of two distinct Fe-Mn-rich rims on the dolomite core was possible. The inner rim has greater Fe and Mn content implying that early diagenetic alkaline porewater chemistry was characterized by higher dissolved Fe^{2+} and Mn^{2+} during the precipitation of the first overgrowth generation. Interestingly, some overgrowths show considerably higher Mn and low Fe content reflecting higher Mn^{2+} concentrations in pore water

relative to Fe^{2+}, particularly in samples from the upper part of the Unit V where in addition to dolomites rare kutnohorite-type carbonate phase occur. These changes in carbonate mineral-chemistry coincides with abrupt increase in bulk rock Mn concentrations.

In contrast to lower units, carbonate phases in Unit VI show that dominantly Mn-rich carbonate cores are mainly close to zoned kutnohorite but also siderite (Figure 12, 13, 14). The outer zones are usually more ankerite-type. This suggest that primary Mn-carbonate phases were probably precipitated in carbonate saturated anoxic sediment/mud enriched in dissolved Mn^{2+}. The outer diagenetic rims are formed in further porewater saturation changing towards Fe-Mn dolomite and precipitating on the Mn-carbonate nucleuses. It is also important the Unit VI is characterized by abundant pyrite framboids, possibly formed by consuming sulphide that is produced by microbial sulphate reduction *(MSR)* and causing fixation of dissolved Fe^{2+}, that in turn leads to Fe(II)-depleted pore water and increase in Mn-carbonate saturation (Petrash et al., 2016).

Mn carbonate precipitation model in LST12 succession

The Mn-enriched dolomite and primary Mn-carbonate precipitation in LST12 succession has occurred in Units V and VI, and to lesser extent in Unit IV. Appearance of Mn-carbonates in LST12 core coincides with facies change from carbonate dominated tidal and shallow-marine (periodically exposed and karstified) settings in Unit I-III to transgression below the storm-wave base and deposition of black-shales interbedded with carbonates in Units IV-VI.

Mn-bearing carbonates typically form during early diagenesis in transitional redox zones of the basin, mainly in settings where strongly reduced deep-water conditions changes towards oxic shallow-water environments (Kuleshov & Maynard, 2019). There are currently three different depositional models (oxic, euxinic or carbonate) proposed with respect to $\delta^{13}C_{DIC}$ and concentrations of dissolved O_2, Fe, Mn and H_2S in the water column (Figure 16). Though the origin of Fe and Mn can be either hydrothermal, derived from springs or be related to the release in sediment porewaters then in all three models a stratified water column with well-defined redoxcline is required (Wittkop et al., 2020).

Low carbonate saturation or elevated contents of dissolved Mn in upwelling systems may indicate the oxic (Oxygen Minimum Zone) model, where the stratification of oxic surface waters and anoxic deeper waters with the formation of redoxcline create conditions for the precipitation of Mn-oxyhydroxides. Reductive conditions caused by degradation of abundant

organic matter produced in upwelling zones drive the dissolution of Mn-oxyhydroxides leading to early diagenetic Mn-carbonate precipitation (Calvert & Pedersen, 1996; Figure 16 c). In this case, the formation of shales is common in the reduced deep water settings (Wittkop et al., 2020).

In carbonate model the water column is characterized by stratified ferruginous depositional settings (Figure 16 a). In this model Mn-oxyhydroxides may not be present if the rate of Mn-carbonate precipitation exceeds the rate of supply. Also, since the active oxygenic photosynthesis was absent in most of the Archean oceans then Mn-oxyhydroxides were not present in Archean, but genesis of manganese oxides become possible by late Archean and Proterozoic. In this model carbonate phases (calcite/dolomite) form in the surface waters and dissolve by settling through lysocline where pH drops below calcite or dolomite equilibrium (Wittkop et al., 2020), and where Mn-carbonates form. In ferruginous deeper waters, the precipitation of Fe-rich overgrowths or siderite can occur.

In the stratified basin of the euxinic model (Force & Cannon, 1988; Herndon et al., 2018; Figure 16 b), Mn-oxyhydroxides may also occur or be absent, and Mn-carbonates precipitate near the redoxcline. However, in the case of high $CaCO_3$ accumulation rates the precipitation of Mn-carbonates can occur throughout the basin. In the sulfidic deeper parts of the basin, iron-sulphides containing black shales form (Wittkop et al., 2020).

In one hand the variable Mn-Fe-Ca(Mg) carbonate composition, petrographic features showing Mn-enriched carbonate precipitation on dolomitic cores in Units IV and V, and Mn-carbonate nucleation with concurrent precipitation and/or replacement with Fe-Mg-Ca carbonate minerals together with siderite implying variable Fe/Mn ratios would call for a carbonate model. On the other hand, direct association of the most Mn-rich carbonates with pyrite rich black shales suggests either euxinic or oxic models being operative during the precipitation of Mn-rich carbonates in Lastoursville basin.

Based on sediment facies characteristics, presence of Fe-sulphides and their appearance as rather large framboidal aggregates, disseminated euhedral crystals, and distribution and characteristics of Mn carbonate minerals in LST12 succession support the oxic model. Under euxinic conditions the pyrite forms already in water column whereas the size distribution of pyrite framboids in euxinic settings has an uniform mean diameter of about 5 μm and larger framboids (>10 μm) are absent (Bond & Wignall, 2010). Framboids of various and larger size form within sediment due to the microbial sulphate reduction. Though the framboids can recrystallize and grow in size during later stages of diagenesis, pyrite framboid aggregates of

>10 μm size and abundant disseminated pyrite euhedral crystallites do not support the euxinic model of Mn-carbonate precipitation in Lastoursville basin and the oxic model is preferred. However, it must be noted that some pyrite aggregates and single crystallites show well defined zonality in BSE images (Figure 8 n) hinting on diagenetic recrystallization and growth. Using EDS analysis it was not possible to recognize any significant differences in major element composition between core and rims in such aggregates and this phenomenon requires further trace element characterization using more sensitive methods.

Given the various contents of Ca-Mg-Fe-Mn of the LST12 core carbonates, the deposition of different Units occurred in stratified environmental settings with different concentrations of manganese, dependent on the influx of Mn^{2+} and the changes in redox conditions. The precipitation of manganese oxyhydroxides and carbonates could suggest the formation in a deepening oxic-anoxic basin where the water masses were separated by shallow redoxcline (Wittkop et al., 2020). Unit I-III are mainly composed of dolostones with occasional more shale dolomarl interlayers, where the primary carbonate phase is a stoichiometric dolomite, suggesting precipitation is shallow oxic environment. This is also in accordance with low total organic concentrations of those Units, mainly less than 1 wt.% (Figure 15). The Fe-Mn-rims on dolomite crystallites in these Units formed during the reductive dissolution of detrital phases and solid Fe-Mn-oxyhydroxides leading to pore fluid saturation with respect to Fe(Mn)-dolomite (Petrash et al., 2016). Units IV to VI were marked by fluctuating depositional environment, where Unit IV is composed of interlayering of organic-rich shale and carbonate beds and Unit V consists mostly dolostones with rhythmic layering. The sedimentological features and composition of Unit VI pyrite-rich shales suggest deeper reduced environment, that is characterized by the dominance of primary Fe-Mn-carbonates along with the first occurrence of siderites. The appearance of Mn-rich carbonates already from Unit V and their prevalence in Unit VI suggest increased Mn concentration, probably provided by upwelling of reduced water masses that contained dissolved Mn (II). Given that and the alternating composition of Unit IV and V, it is possible that these units formed close to redoxcline, where Mn-oxyhydroxides were formed above the redoxcline using Mn (II) that was brought by upwelling anoxic waters, followed by diagenetic (microbial) reduction of oxides-hydroxides within sediment and precipitation of Mn-carbonates (Calvert & Pedersen, 1996) whereas the absence of Mn(Fe)-oxyhydroxide precipitates in this succession indicates that the reduction rates exceeded the Mn supply.

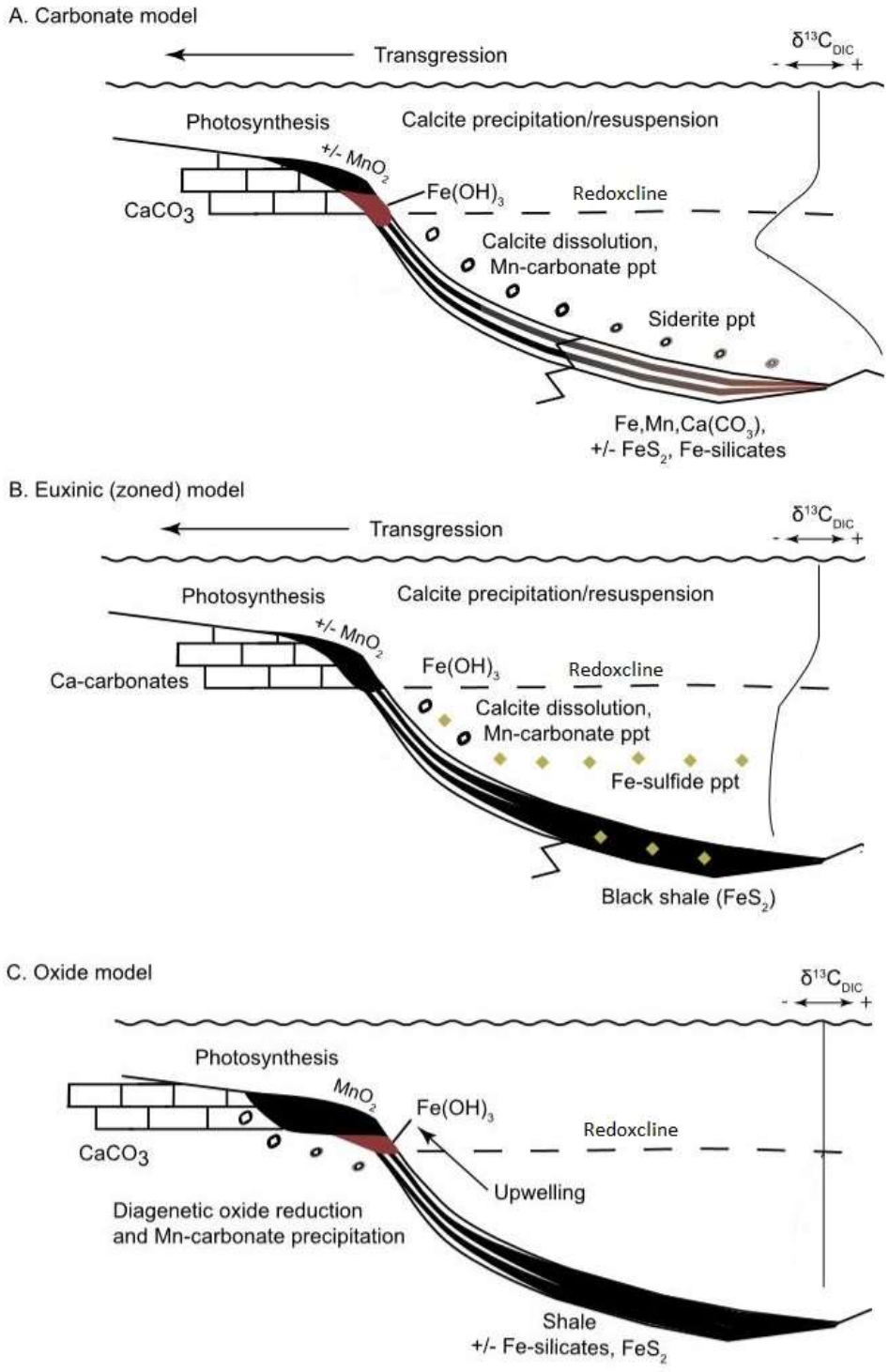

Figure 16. Models for the formation environments of sedimentary manganese deposits. Modified after Wittkop et al. (2020).

Bacterial influence on manganese precipitation

The formation of Mn minerals in sediments is a biogeochemical process, where, in addition to molecular oxygen, bacterial activity plays an essential role. As Mn (II) is an important nutrient for planktonic productivity, bacterial oxidation is thought to control the contents of dissolved Mn (II) in oceans (Polgári et al., 2012). Fixation of manganese into sedimentary deposits by oxidation of mobile Mn (II) to Mn(III,IV)oxides and further formation of Mn-carbonates by reduction of Mn(IV)oxides are mediated by microbial activity (Tebo et al., 2004; Johnson et al., 2016). Microorganisms (bacteria, fungi) that participate in enzymatic manganese oxidation of Mn (II) to Mn (III,IV) are widespread. Due to the surface-catalysed reactions, bacterial Mn (II) oxidation processes are much faster than abiotic Mn (II) oxidation (Tebo et al., 2004). The evidence of microbial role in Mn metallogenesis has been well established (Fan et al., 1999; Polgári et al., 2012a; Polgari et al., 2012b). Common feature in various deposits is the presence of fine, organic-rich microlaminae with thin "crinkly" bedding that is typical for microbially-induced sedimentary structures (Polgári et al., 2014), whereas the depositional environment for Mn-carbonate bearing black shales are suggested to be low-temperature bacterially mediated system of non-sulphidic-oxic setting (Polgári et al., 2004).

Similar features observed in Unit VI black shales suggest involvement of bacterial processes during deposition of Mn-carbonate rich interlayers-lenses. It is interesting that Mn-rich Unit V is characterized by low pyrite (and S) content but high Fe/Al and Mn/Al ratio (Figure 11) suggesting that both Fe and Mn are in carbonate fraction and the depositional environment did not reached the sulphate reduction zone where sulphide and Fe^{2+} would have been removed by pyrite precipitation. Hence, abundant MnO_2 was utilized as an electron donor for organic matter mineralization instead. In contrast, Unit VI primary Mn-carbonate phases co-occur with abundant pyrite in anoxic sediment/mud enriched in dissolved Mn^{2+} suggesting that the early diagenetic microbial sulphate and MnO_2 reduction were operating together (Neumann et al., 2002). The presence of abundant pyrite framboids explains the fixation of Fe^{2+} from pore waters in sulphate-reductive anoxic environment and saturation with respect of Mn-carbonate phase in this Unit and also in Unit IV.

High TOC contents in Unit IV and VI also suggest the upwelling of oxygen-depleted and nutrient-rich waters. TOC concentrations are typically highest in sediments deposited within perennial anoxic OMZ (median = 10.5 wt.%) whereas median TOC concentrations in other environments are in the range of 2.0–4.7 wt.% (Bennett et al., 2020). The TOC contents in Unit IV and VI reach up to 14.1% (Figure 15) exceeding median TOC concentrations within anoxic

core of perennial OMZ (10.5 wt.%). The occurrence of high TOC concentrations in Unit IV and VI reflect the presence of environment of anoxic perennial OMZ, beneath perennial OMZ or euxinic.

The same interpretation can be made using redox-sensitive trace elements such as vanadium (V), uranium (U), molybdenum (Mo), rhenium (Re), cobalt, (Co), nickel (Ni), chromium (Cr) that are extensively used as redox proxies to infer paleo-redox conditions of ancient sediments. Using trace element enrichment values, it is possible to differentiate various marine depositional environments such as euxinic basins, continental margin upwelling settings and normal oxic settings (e.g., Algeo & Tribovillard, 2009; Bennett et al., 2020; Scholz, 2018; Tribovillard et al., 2006; Tribovillard et al., 2012; Zhang et al., 2016). Most recently Bennet et al. (2020) have shown that V, U, Mo and Re are the most useful with enrichments of Mo < 0.4 ppm/% and Re < 1.3 ppb/% show oxic environment, while U (> 1 ppm/%), V (< 23 ppm /%) and Mo (< 5 ppm/%) infer to oxic water beneath the core of a perennial OMZ depositional system; in euxinic environment enrichments of trace metals are in range of Mo (> 5.0 ppm/%) and V (46 - 23 ppm/%); the largest enrichments are present under anoxic conditions in perennial OMZ environment with V > 46 ppm/%, U > 5 ppm/% and Mo > 5 ppm/% (Figure 17). However, it is important to note that molybdenum alone shows similar enrichments in various environments and therefore it cannot be used as a paleo-redox tracer alone. Similarly, uranium together with vanadium gives the most useful paleo-redox information, since their enrichment combination is unique to sediments in various environments (Bennett et al., 2020).

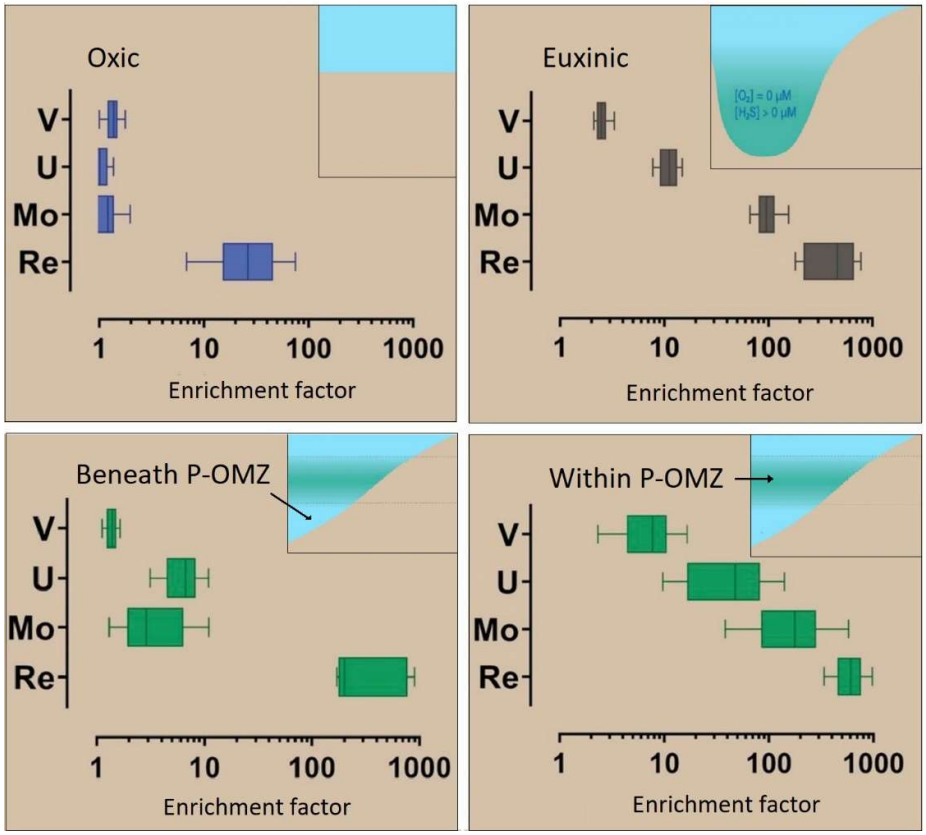

Figure 17. Trace element enrichment factors in euxinic basin, perennial OMZ and oxic sedimentary environments. Modified after Bennett et al., (2020).

Trace element concentrations normalized to Al in Unit I, II, III and V of the LST12 core are mainly U > 1, V < 23 and Mo < 0.4 ppm/% and therefore refer to oxic depositional environment of these Units (Figure 18, 19). However, trace element concentrations in some intervals of Unit III and V are slightly higher and may indicate transient euxinic environments or settings beneath perennial OMZ. In Unit IV and VI, mainly composed of shales, the concentrations of trace elements are in the range of V ≥ 23, Mo > 0.4 and U > 1 ppm/% in Unit V, while in Unit VI the enrichments are for V ≥ 23 ppm/%, higher or close to U > 1 ppm/% but half of the enrichment values for Mo are > 0.4 ppm/%. These systematically different values compared with trace element enrichments in other Units suggest alternation of euxinic and beneath perennial OMZ environments during deposition of Units IV and VI (Figure 18, 19).

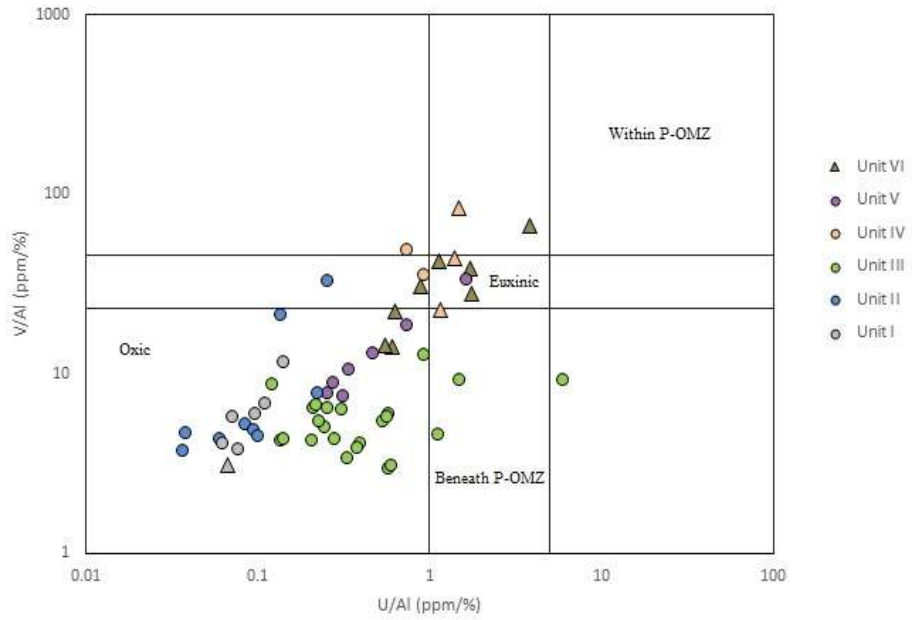

Figure 18. Vanadium enrichments against uranium enrichments normalized to aluminium concentration. Shales are marked with a triangle.

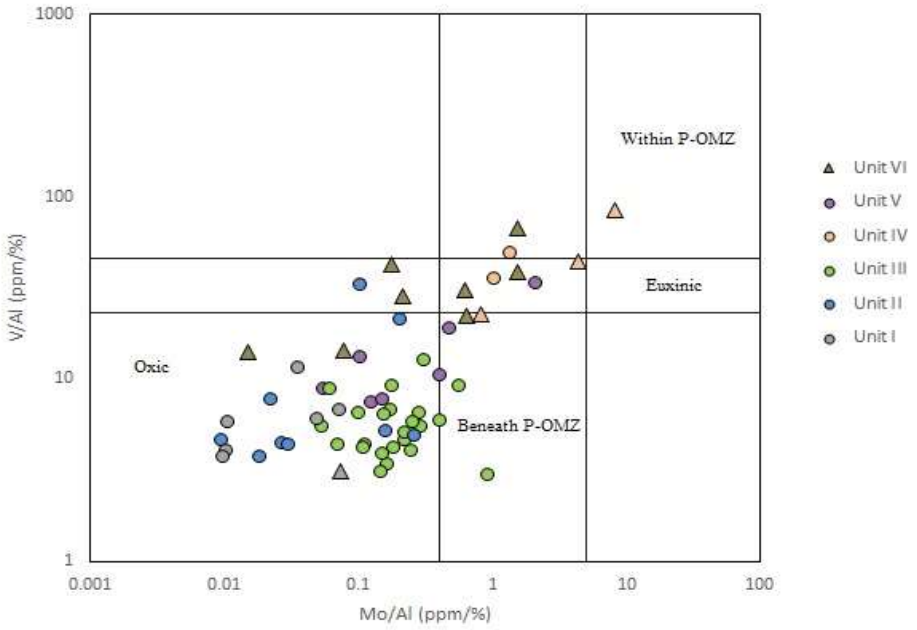

Figure 19. Vanadium enrichments against molybdenum enrichments normalized to aluminium. Shales are marked with a triangle.

Similar conclusion can be also drawn from trace element enrichment trends based on enrichment factors (EF), that describe the enrichments of V, Mo, U and Re above the crustal

average (Figure 20). Due to the low detrital concentration of rhenium, it exhibits the highest trace element enrichment factors in depositional environments. Since vanadium concentrations in the Earth's crust are noteworthy, it usually shows the lowest enrichments above the average. In normal oxic environment, the enrichment factors of V, U and Mo are minor and typically slightly higher or equal to (≥) 1, whereas EF of Re is in range of 10–100. Enrichment factor values of trace elements depositing in settings beneath OMZ are somewhat higher and are in enrichment values range of approximately V_{EF}≥1, Mo_{EF}=1–10 and U_{EF}<10. The largest trace element enrichments above the crustal average are observed in environments within the OMZ, where V_{EF}≥10, U_{EF}=10–100 and Mo_{EF}>100; in euxinic environment, enrichment factors are slightly lower with values of approximately V_{EF}=1–10, U_{EF}=10 and Mo_{EF}=100. In euxinic environment and settings within and beneath OMZ, values range of Re_{EF}=100–1000 (Bennett et al., 2020). Based on Figure 20, Unit I, II, III and V exhibits minor enrichments of V, U and Mo relative to crustal average and, therefore, can be interpreted as an oxic environment. Enrichment factors of V, Mo, U and Re in Unit IV and VI shales infer to enrichments under conditions either in euxinic settings or most likely in environment beneath OMZ.

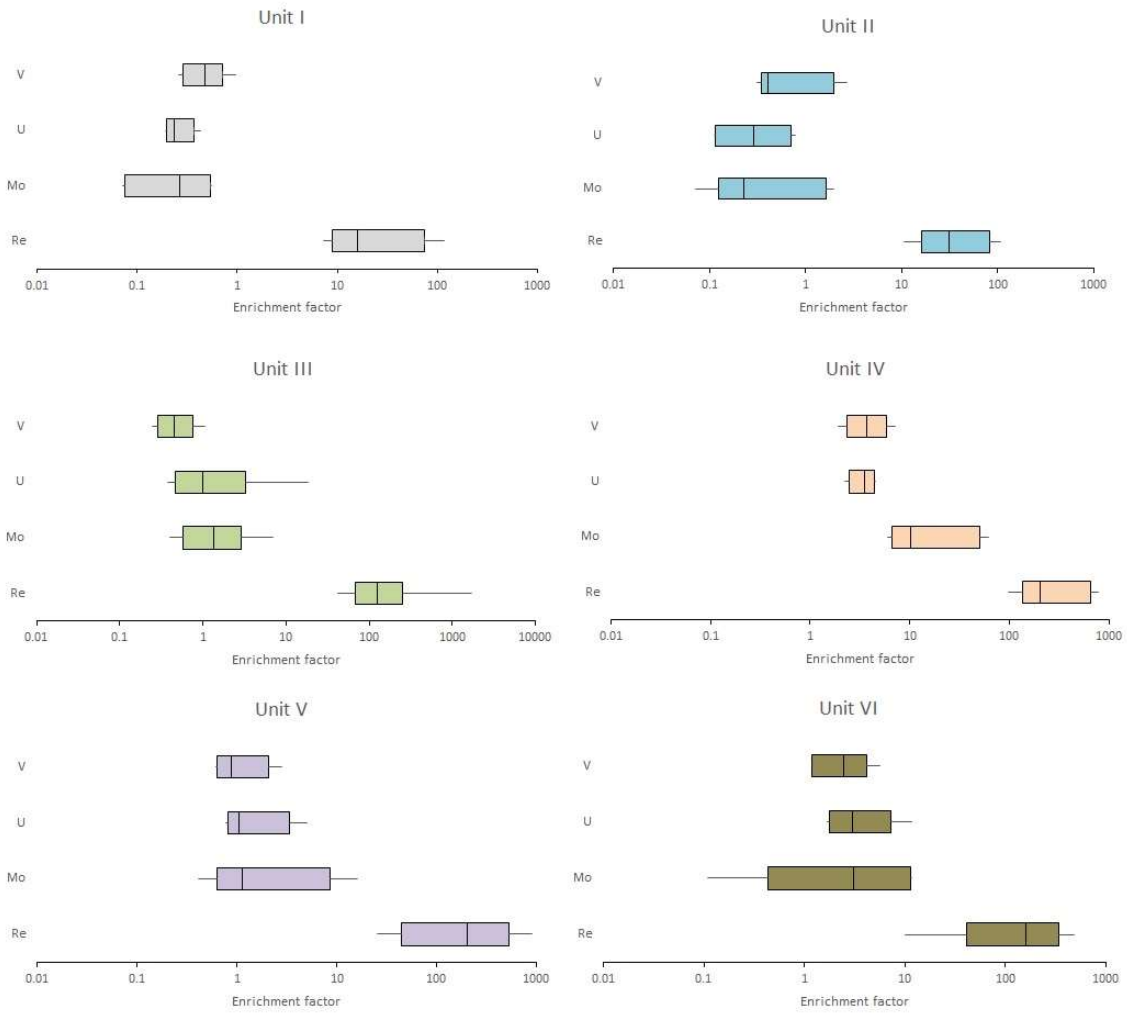

Figure 20. Trace element V, U, Mo and Re enrichment factors (EF) of Unit I-VI. Enrichment factors are plotted as box and whisker plots in interquartile range, where the whiskers represent the 10^{th} and 90^{th} percentiles. The mean of each unit is shown as a stripe.

Summary and Conclusions

The aim of this study was to describe the petrography, mineralogical and geochemical composition of Mn-bearing carbonates in the 139 m long LST12 core succession from Palaeoproterozoic Francevillian Lastoursville sub-basin in Gabon. Using the bulk geochemical and mineralogical data combined with trace element enrichment and total organic carbon (TOC) trends, it was possible to interpret the changes in redox conditions during the deposition of Mn-rich carbonates and black shales of the LST12 core. The petrography, microstructure of the carbonate phases and distribution of major elements in different Units were described using optical and scanning electron microscope (SEM).

Unit I-III are mainly composed of dolostones with occasional shaly dolomarl interlayers. Primary carbonate phase represented by stoichiometric dolomite with low TOC concentrations and minor trace element enrichment factors of these Units suggest shallow oxic depositional environment during the deposition of Unit I-III. Precipitation of thin Fe-Mn-rich rims on stoichiometric dolomite core formed due to the pore fluid saturation of Fe(Mn)-dolomite, possibly caused by the reductive dissolution of Fe-Mn-oxyhydroxides.

Unit IV is composed of pyrite-rich black shales with interlayering of dolomarls, whereas Unit V of dolo-rhytmites where Mn-carbonates start to appear. Carbonates of these Units are characterized by dolomite cores with well-defined and wide rims, where the precipitation occurred at high carbonate saturation levels and in Fe-Mn-enriched fluid possibly changing in composition over the time supported by several distinct Fe-Mn-rich rims. These Units possibly formed at fluctuating redoxcline, where Mn-carbonates precipitated through diagenetic (microbial) reduction of Mn-oxyhydroxides.

The composition and sedimentological characteristics suggest that pyrite-rich Unit VI shales formed in deeper reduced environment. Primary dominant carbonate phases in Unit VI are characterized by Mn-carbonate cores close to kutnohorite, that were probably precipitated in carbonate saturated anoxic sediment/mud enriched in dissolved Mn^{2+}, with further porewater saturation changing towards Fe-Mn-dolomite, causing the precipitation of Fe-Mn rims on Mn-carbonate nucleus. Microlaminae features observed in Unit VI black shales suggest bacterial processes during the deposition of Mn-carbonate rich lens-like interlayers. The Mn-carbonates of Unit VI co-occur with abundant pyrite framboids, possibly formed by microbial sulphate reduction. Values of high TOC concentrations and trace element enrichment factors reflect the alternation of euxinic setting and environment beneath perennial OMZ for Units IV and VI.

The chemical and mineralogical composition of Mn carbonate minerals, sediment facies and presence of large framboidal pyrite aggregates in LST12 succession support the oxic model as a deepening basin, where the oxic surface water and deep anoxic water were separated by shallow redoxcline, influenced by variable influx of Mn^{2+}.

Acknowledgments

I would like to thank Aivo Lepland and Tony Prave for their guidance. Special thanks go to colleagues at the Masuku University, Franceville, especially Alexis Ndongo, Mathieu Moussavou, Karen Bakakas and Michel Mbina for the warm welcome, undiscribable help in Franceville and sample collection as well as the Erasmus+ scholarship for giving me the opportunity to study the geology of Gabon on sight. In addition, I appreciate all the previously done work, effort and help in collecting and measuring the LST12 core samples.

References

Albani, A. El, Bengtson, S., Canfield, D. E., Bekker, A., MacChiarelli, R., Mazurier, A., Hammarlund, E. U., Boulvais, P., Dupuy, J. J., Fontaine, C., Fürsich, F. T., Gauthier-Lafaye, F., Janvier, P., Javaux, E., Ossa, F. O., Pierson-Wickmann, A. C., Riboulleau, A., Sardini, P., Vachard, D., … Meunier, A. (2010). Large colonial organisms with coordinated growth in oxygenated environments 2.1 Gyr ago. *Nature*, *466*(7302), 100–104. https://doi.org/10.1038/nature09166

Algeo, T. J., & Tribovillard, N. (2009). Environmental analysis of paleoceanographic systems based on molybdenum-uranium covariation. *Chemical Geology*, *268*(3–4), 211–225. https://doi.org/10.1016/j.chemgeo.2009.09.001

Azzibrouck, A. (1986). *SEDIMENTOLOGIE ET GEOCHIMIE DU FRANCEVILLIEN B (PROTEROZOIQUE INFERIEUR). METALLOGENIE DES GISEMENTS DE MANGANESE DE MOANDA, GABON* (p. 220).

Bankole, O. M., El Albani, A., Meunier, A., Rouxel, O. J., Gauthier-Lafaye, F., & Bekker, A. (2016). Origin of red beds in the paleoproterozoic Franceville Basin, Gabon, and implications for sandstone-hosted uranium mineralization. *American Journal of Science*, *316*(9), 839–872. https://doi.org/10.2475/09.2016.02

Bekker, A., Holland, H. D., Wang, P. L., Rumble, D., Stein, H. J., Hannah, J. L., Coetzee, L. L., & Beukes, N. J. (2004). Dating the rise of atmospheric oxygen. *Nature*, *427*(6970), 117–120. https://doi.org/10.1038/nature02260

Bennett, W. W., Canfield, D. E., Pre-proof, J., & Bennett, W. W. (2020). Redox-sensitive trace metals as paleoredox proxies: A review and analysis of data from modern sediments. *Earth-Science Reviews*, 103175. https://doi.org/10.1016/j.earscirev.2020.103175

Beukes, N. J., Swindell, E. P. W., & Wabo, H. (2016). Manganese deposits of Africa. *Episodes*, *39*(2), 285–317. https://doi.org/10.18814/epiiugs/2016/v39i2/95779

Bond, D. P. G., & Wignall, P. B. (2010). Pyrite framboid study of marine Permian-Triassic boundary sections: A complex anoxic event and its relationship to contemporaneous mass extinction. *Bulletin of the Geological Society of America*, *122*(7–8), 1265–1279. https://doi.org/10.1130/B30042.1

Calvert, S. E., & Pedersen, T. F. (1996). Sedimentary geochemistry of manganese:

Implications for the environment of formation of manganiferous black shales. *Economic Geology*, *91*(1), 36–47. https://doi.org/10.2113/gsecongeo.91.1.36

Dubois, M. (2017). *Environnement de dépôt et processus de formation des carbonates de manganèse dans les black shales paléoprotérozoiques du Bassin de Franceville (2 . 1 Ga ; Gabon) To cite this version : HAL Id : tel-01621460*.

Dubois, M., Lopez, M., Orberger, B., Gay, A., Moussavou, M., Pambo, F., & Rodrigues, S. (2017). The 2.1 Ga-old injectite network of the Franceville Basin, Gabon: Architecture, origin and implications on manganese mineralization. *Precambrian Research*, *302*(September), 255–278. https://doi.org/10.1016/j.precamres.2017.09.022

Dubois, M., Lopez, M., Orberger, B., Rodriguez, C., Boussafir, M., Dreux, G., Rodrigues, S., & Pambo, F. (2015). The Mn-Carbonate Rich Black Shales of the Bangombe Plateau, Francevillian Basin, Gabon. *13th Biennial SGA Meeting*, 1905–1908.

Fan, D., Ye, J., Yin, L., & Zhang, R. (1999). Microbial processes in the formation of the Sinian Gaoyan manganese carbonate ore, Sichuan Province, China. *Ore Geology Reviews*, *15*(1–3), 79–93. https://doi.org/10.1016/S0169-1368(99)00016-5

Force, E. R., & Cannon, W. F. (1988). Depositional model for shallow- marine manganese deposits around black shale basins. *Economic Geology*, *83*(1), 93–117. https://doi.org/10.2113/gsecongeo.83.1.93

Gauthier-Lafaye, F., & Weber, F. (2003). Natural nuclear fission reactors: Time constraints for occurrence, and their relation to uranium and manganese deposits and to the evolution of the atmosphere. *Precambrian Research*, *120*(1–2), 81–100. https://doi.org/10.1016/S0301-9268(02)00163-8

Gumsley, A. P., Chamberlain, K. R., Bleeker, W., Söderlund, U., De Kock, M. O., Larsson, E. R., & Bekker, A. (2017). Timing and tempo of the great oxidation event. *Proceedings of the National Academy of Sciences of the United States of America*, *114*(8), 1811–1816. https://doi.org/10.1073/pnas.1608824114

Herndon, E. M., Havig, J. R., Singer, D. M., McCormick, M. L., & Kump, L. R. (2018). Manganese and iron geochemistry in sediments underlying the redox-stratified Fayetteville Green Lake. *Geochimica et Cosmochimica Acta*, *231*, 50–63. https://doi.org/10.1016/j.gca.2018.04.013

Holland, H. D. (2006). The oxygenation of the atmosphere and oceans. *Philosophical*

Transactions of the Royal Society B: Biological Sciences, *361*(1470), 903–915. https://doi.org/10.1098/rstb.2006.1838

Horie, K., Hidaka, H., & Gauthier-LaFaye, F. (2005). U-Pb geochronology and geochemistry of zircon from the Franceville series at Bidoudouma, Gabon. *Geochimica et Cosmochimica Acta*, *69*(10), A11–A11. isi:000229399700022

Johnson, J. E., Webb, S. M., Ma, C., & Fischer, W. W. (2016). Manganese mineralogy and diagenesis in the sedimentary rock record. *Geochimica et Cosmochimica Acta*, *173*, 210–231. https://doi.org/10.1016/j.gca.2015.10.027

Kuleshov, V., & Maynard, J. (2019). Isotope geochemistry - The Origin and Formation of Manganese Rocks and Ores. In *Journal of Chemical Information and Modeling* (Vol. 53, Issue 9). https://doi.org/10.1017/CBO9781107415324.004

Maynard, J. Barry. (2010). The chemistry of manganese ores through time: A signal of increasing diversity of earth-surface environments. *Economic Geology*, *105*(3), 535–552. https://doi.org/10.2113/gsecongeo.105.3.535

Maynard, J B, & Force, E. R. (1991). Manganese : Syngenetic deposits on the margins of anoxic basins Chapter 11. *Reviews on Economic Geology*, *5*(March), 147–157.

Mouélé, I. M., Dudoignon, P., El Albani, A., Meunier, A., Boulvais, P., Gauthier-Lafaye, F., Paquette, J. L., Martin, H., & Cuney, M. (2014). 2.9-1.9Ga paleoalterations of Archean granitic basement of the Franceville basin (Gabon). *Journal of African Earth Sciences*, *97*, 244–260. https://doi.org/10.1016/j.jafrearsci.2014.04.027

Moussavou, M., Edou-Minko, A., Mounguengui, M., Ortega, R., Fleury, G., Roudeau, S., Carmona, A., Genty, D., Blamart, D., Tchikoundzi, C., Mvoubou, M., & Musavu-Moussavou, B. (2015). *Multicellular Consortia Preserved in Biogenic Ductile-Plastic Nodules of Geology & Geosciences Multicellular Consortia Preserved in Biogenic Ductile-Plastic Nodules of*. *July*. https://doi.org/10.13140/RG.2.1.3680.6248

Ndongo, A., Guiraud, M., Vennin, E., Mbina, M., Buoncristiani, J. F., Thomazo, C., & Flotté, N. (2016). Control of fluid-pressure on early deformation structures in the Paleoproterozoic extensional Franceville Basin (SE Gabon). *Precambrian Research*, *277*, 1–25. https://doi.org/10.1016/j.precamres.2016.02.003

Neumann, T., Heiser, U., Leosson, M. A., & Kersten, M. (2002). Early diagenetic processes during Mn-carbonate formation: Evidence from the isotopic composition of authigenic

Ca-rhodochrosites of the Baltic Sea. *Geochimica et Cosmochimica Acta*, *66*(5), 867–879. https://doi.org/10.1016/S0016-7037(01)00819-5

Ossa, F. O., Eickmann, B., Hofmann, A., Planavsky, N. J., Asael, D., Pambo, F., & Bekker, A. (2018). Two-step deoxygenation at the end of the Paleoproterozoic Lomagundi Event. *Earth and Planetary Science Letters*, *486*, 70–83. https://doi.org/10.1016/j.epsl.2018.01.009

Ossa Ossa, F., El Albani, A., Hofmann, A., Bekker, A., Gauthier-Lafaye, F., Pambo, F., Meunier, A., Fontaine, C., Boulvais, P., Pierson-Wickmann, A. C., Cavalazzi, B., & Macchiarelli, R. (2013). Exceptional preservation of expandable clay minerals in the ca. 2.1Ga black shales of the Francevillian basin, Gabon and its implication for atmospheric oxygen accumulation. *Chemical Geology*, *362*, 181–192. https://doi.org/10.1016/j.chemgeo.2013.08.011

Pambo, F. (2004). *Conditions de formation des carbonates de manganèse protézoïques et analyse minéralogique et géochimique des minerais à bioxydes de manganèse associés dans le gisement de Moanda (Sud-Est, Gabon)* (p. 274).

Petrash, D. A., Gueneli, N., Brocks, J. J., Méndez-Dot, J. A., González-Arismendi, G., Poulton, S. W., & Konhauser, K. O. (2016). Black shale deposition and early diagenetic dolomite cementation during Oceanic Anoxic Event 1: The mid-Cretaceous Maracaibo Platform, Northwestern South America. *American Journal of Science*, *316*(7), 669–711. https://doi.org/10.2475/07.2016.03

Petrash, D. A., Lalonde, S. V., González-Arismendi, G., Gordon, R. A., Méndez, J. A., Gingras, M. K., & Konhauser, K. O. (2015). Can Mn-S redox cycling drive sedimentary dolomite formation? A hypothesis. *Chemical Geology*, *404*(February 2018), 27–40. https://doi.org/10.1016/j.chemgeo.2015.03.017

Polgari, M., Hein, J. R., Toth, A. L., Pal-Molnár, E., Vigh, T., Biró, L., & Fintor, K. (2012). Microbial action formed Jurassic Mn-carbonate ore deposit in only a few hundred years (Úrkút, Hungary). *Geology*, *40*(10), 903–906. https://doi.org/10.1130/G33304.1

Polgári, M, Hein, J. R., Vigh, T., Szabó-drubina, M., Fórizs, I., Bíró, L., Müller, A., & Tóth, A. L. (2012). Microbial processes and the origin of the Úrkút manganese deposit , Hungary. *Ore Geology Reviews*, *47*, 87–109. https://doi.org/10.1016/j.oregeorev.2011.10.001

Polgári, Márta, Németh, T., Pál-molnár, E., Futó, I., Vigh, T., & Mojzsis, S. J. (2014).

Correlated chemostratigraphy of Mn-carbonate microbialites (Úrkút , Hungary). *Gondwana Research*, *29*(1), 278–289. https://doi.org/10.1016/j.gr.2014.12.002

Polgári, Márta, Szabó-Drubina, M., & Szbó, Z. (2004). Theoretical model for Jurassic manganese mineralization in Central Europe, Úrkút, Hungary. *Bulletin of Geosciences*, *79*(1), 53–61. https://doi.org/10.3140/bull.geosci.2004.01.053

Préat, A., Bouton, P., Thiéblemont, D., Prian, J. P., Ndounze, S. S., & Delpomdor, F. (2011). Paleoproterozoic high δ13C dolomites from the Lastoursville and Franceville basins (SE Gabon): Stratigraphic and synsedimentary subsidence implications. *Precambrian Research*, *189*(1–2), 212–228. https://doi.org/10.1016/j.precamres.2011.05.013

Reynaud, J. Y., Trentesaux, A., El Albani, A., Aubineau, J., Ngombi-Pemba, L., Guiyeligou, G., Bouton, P., Gauthier-Lafaye, F., & Weber, F. (2018). Depositional setting of the 2·1 Ga Francevillian macrobiota (Gabon): Rapid mud settling in a shallow basin swept by high-density sand flows. *Sedimentology*, *65*(3), 670–701. https://doi.org/10.1111/sed.12398

Rudnick, R. L., & Gao, S. (2014). Composition of the Continental Crust. In *Treatise on Geochemistry* (2nd ed.). Elsevier Ltd. https://doi.org/10.1016/B978-0-08-095975-7.00301-6

Sawaki, Y., Moussavou, M., Sato, T., Suzuki, K., Ligna, C., Asanuma, H., Sakata, S., Obayashi, H., Hirata, T., & Edou-Minko, A. (2017). Chronological constraints on the Paleoproterozoic Francevillian Group in Gabon. *Geoscience Frontiers*, *8*(2), 397–407. https://doi.org/10.1016/j.gsf.2016.10.001

Scholz, F. (2018). Identifying oxygen minimum zone-type biogeochemical cycling in Earth history using inorganic geochemical proxies. *Earth-Science Reviews*, *184*(August 2018), 29–45. https://doi.org/10.1016/j.earscirev.2018.08.002

Swart, P. K. (2015). The geochemistry of carbonate diagenesis: The past, present and future. *Sedimentology*, *62*(5), 1233–1304. https://doi.org/10.1111/sed.12205

Tebo, B. M., Bargar, J. R., Clement, B. G., Dick, G. J., Murray, K. J., Parker, D., Verity, R., & Webb, S. M. (2004). BIOGENIC MANGANESE OXIDES: Properties and Mechanisms of Formation. *Annual Review of Earth and Planetary Sciences*, *32*(1), 287–328. https://doi.org/10.1146/annurev.earth.32.101802.120213

Tribovillard, N., Algeo, T. J., Baudin, F., & Riboulleau, A. (2012). Analysis of marine

environmental conditions based onmolybdenum-uranium covariation-Applications to Mesozoic paleoceanography. *Chemical Geology*, *324–325*, 46–58. https://doi.org/10.1016/j.chemgeo.2011.09.009

Tribovillard, Nicolas, Algeo, T. J., Lyons, T., & Riboulleau, A. (2006). Trace metals as paleoredox and paleoproductivity proxies: An update. *Chemical Geology*, *232*(1–2), 12–32. https://doi.org/10.1016/j.chemgeo.2006.02.012

Vahrenkamp, V. C., & Swart, P. K. (1994). Late Cenozoic dolomites of the Bahamas: metastable analogues for the genesis of ancient platform dolomites. *Dolomites: A Volume in Honour of Dolomieu*, *January*, 133–153. https://doi.org/10.1002/9781444304077.ch9

Weber, F. (1968). *Une série précambrienne du Gabon : le France-villien. Sédimentologie, géochimie, relations avec les gîtes minéraux associés.*

Weber, F., & Gauthier-Lafaye, F. (2013). No proof from carbon isotopes in the Francevillian (Gabon) and Onega (Fennoscandian shield) basins of a global oxidation event at 1980-2090 Ma following the Great Oxidation Event (GOE). *Comptes Rendus - Geoscience*, *345*(1), 28–35. https://doi.org/10.1016/j.crte.2012.12.003

Wittkop, C., Swanner, E. D., Grengs, A., Lambrecht, N., Fakhraee, M., Myrbo, A., Bray, A. W., Poulton, S. W., & Katsev, S. (2020). Evaluating a primary carbonate pathway for manganese enrichments in reducing environments. *Earth and Planetary Science Letters*, *538*, 116201. https://doi.org/10.1016/j.epsl.2020.116201

Zhang, S., Wang, X., Wang, H., Bjerrum, C. J., Hammarlund, E. U., Costa, M. M., Connelly, J. N., Zhang, B., Su, J., & Canfield, D. E. (2016). Sufficient oxygen for animal respiration 1,400 million years ago. *Proceedings of the National Academy of Sciences of the United States of America*, *113*(7), 1731–1736. https://doi.org/10.1073/pnas.1523449113

Mn-karbonaatide moodustumine Paleoproterosoikumi karbonaatide – mustade kiltade läbilõikes Lastoursville alam-basseinis

Hele-Riin Juhkama

Kokkuvõte

Käesoleva töö eesmärgiks oli iseloomustada Mn-karbonaatide petrograafiat, mineraloogilist ja geokeemilist koostist Lastoursville basseini Paleoproterosoiliste Mn-rikaste dolokivide ja mustade kiltade läbilõikes, mis on avatud 139 m pikkuses LST12 puursüdamikus. Karbonaatide keemilise ja mineraloogilise koostise, jälgelementide rikastumise (V, Mo, U, Re) ning orgaanilise süsiniku (TOC) sisalduse alusel interpreteeriti muutusi Mn-karbonaatide ja mustade kiltade settimisaegse paleokeskkonna redokstingimustes. Karbonaatide petrograafiat, mikrostruktuuri ja põhielementide levikut erinevates puursüdamiku läbilõikes eraldatud üksustes uuriti optilise mikroskoopia ja skaneeriva elektronmikroskoopia (SEM) meetodil.

Mn-karbonaatide keemilise ja mineraloogilise koostise, läbilõikes avatud setendite ja suure (>10 µm) läbimõõduga framboidsete püriidi agregaatide esinemise alusel võib järeldada, et Mn-rikkad karbonaadid LST12 läbilõikes moodustusid transgressiivses basseinis Mn setendite tekkimise nn oksilise mudeli tingimustes, kus madal hapnikurikas vesi ning sügav anoksiline veemass on eraldatud järsu redokskliiniga, milles toimub redutseerivates tingimustes mobiilse Mn^{2+} settimine Mn(Fe) oksiidide-hüdroksiididena ning nende redutseerumine ja Mn-karbonaatide moodustumine vara-diageneesil.

Läbilõikes eraldatud kihid I-III koosnevad peamiselt dolomiitidest vahelduvate savikamate dolokividega. Primaarne stöhhiomeetriline dolomiit, madalad TOC sisaldused ja jälgelementide rikastumisfaktorid viitavad madalale hapnikulisele settekeskkonnale. Fe-Mn-rikkad äärised moodustusid hilisemal poorivee küllastumisel Fe(Mn)-dolomiidi suhtes, mis oli tingitud Fe-Mn-oksühüdroksiidide reduktiivsest lahustumisest.

Neljanda kihi setendid on esindatud püriidirikaste mustade kiltadega, mis vahelduvad savikamate dolokividega, ning V kiht rütmiliste dolokividega, millele on iseloomulik Mn-karbonaatide ilmumine. IV ja V kihi karbonaate iseloomustab dolomiitne tuum laiade ja selgepiiriliste Fe-Mn rikaste ülekasvetega. Need karbonaadid on moodustunud kõrge karbonaatse küllastuse ning Fe-Mn-rikaste fluidide keskkonnas, kus poorivee koostise muutumisel on tekkinud erineva Fe/Mn vahekorraga äärised. Kihid IV ja V moodustusid arvatavasti redokskliinil, kus toimus Mn-oksiidide settimine Mn-rikaste redutseeritud

veemasside tõusuhoovuste (*up-welling*) segunemisel hapnikuliste pinnavetega, samas kui Mn-karbonaadid settisid vara-diageenetilisel (mikroobsel) Mn-oksühüdroksiidide redutseerimisel.

Kihi VI püriidirikaste kiltade koostis ja sedimentoloogilised tunnused viitavad redutseeritud sügavale tekkekeskkonnale. Primaarne domineeriv karbonaatne faas on Mn-rikas tuum, mis koostiselt on sarnane kuthnohoriidile ning mille kõrval esineb ka sideriidile sarnane Fe-karbonaat. Tõenäoliselt toimus nende settimine karbonaatselt küllastunud anoksilises mangaani- ja rauarikkas settes/mudas ning hilisemas poorivee küllastuse rikastumises Fe-Mn-dolomiidi suhtes, mis soodustas Fe-Mn ülekasveid mangaanirikkale tuumale. Kihi VI mustasid kiltasid iseloomustavad mikrolaminaarsed orgaanikarikkad vahekihid ja läätsed, mis viitvad bakteriaalsete protsesside osalusele Mn-oksiidide redutseerimisel ning Mn-karbonaadi rikaste läätseliste kihtide tekkimisel. Kihi VI Mn-karbonaadid esinevad koos rohkete püriidi framboididega, mis tekkisid mikroobsel sulfaadi redutseerimisel. Kõrged orgaanilise ainese (TOC) sisaldused ning jälgelementide rikastumisfaktorid kihis IV ja VI peegeldavad vahelduvat euksiinilist ja/või keskkonda allpool hapniku miinimumtsooni.

Appendix

Table 1. Depth and mineralogy of the LST12 core samples.

Sample	depth (m)	Quartz (wt.%)	K-feldspar (wt.%)	Plagioclase (wt.%)	Chlorite (wt.%)	K-mica (wt.%)	Kaolinite (wt.%)	Calcite (wt.%)	Dolomite (wt.%)	Siderite (wt.%)	Pyrite (wt.%)	Apatite (wt.%)
LST12-1	17.2	42.4	5.3	26.9	9.1	9.3	6.3		0.5			
LST12-BS-1	24.6	48.3	1.6	1.0		23.0	3.7		tr.		##	
LST12-BS-2	25.1	51.7	1.8	4.4		32.8	3.1		1.9	3.6	0.7	
LST12-2	25.9	48.0	3.1	2.6		37.9	3.0		1.5	3.3	0.6	
LST12-BS-3	26.5	57.0	4.8	4.7		26.8	4.0		1.1	0.8	0.6	
LST12-BS-4	26.9	52.6	2.2	6.5		24.6	2.9		9.8	tr.	0.9	
LST12-4b	26.9	55.3	3.4	6.2	2.5	27.4	3.8		0.7		tr.	
LST12-BS-5	27.4	66.8	0.8	1.5		10.6	4.1		10.3	0.5	5.4	
LST12-3b	27.5	51.0	4.5	2.7		30.5	2.9		2.3	5.9		
LST12-3	26.7	54.0	5.8	3.6		31.4	3.2		0.6	0.9	0.6	
LST12-BS-6	28.4	54.0	0.7	7.6		22.8	2.2	tr.	9.5		1.9	
LST12-4	29.0	51.0	3.0	5.4		27.3	2.6		9.5	tr.	0.7	
LST12-BS-7	29.1	56.0	1.6	6.1		25.3	3.0		5.8		0.9	
LST12-BS-8	30.3	72.4	0.7	3.9		17.6	2.5		2.1	tr.	tr.	
LST12-BS-9	30.8	56.2	0.7	6.8		25.0			2.8	5.2	2.2	
LST12-BS-10	31.4	49.2	0.9	5.8		23.0			11.4	3.5	4.2	
LST12-BS-11	31.8	41.9	7.4	9.9	2.2	28.9			1.0	2.0	4.8	
LST12-12bH	32.5	62.5	3.3	0.9		5.1			22.0	4.5		1.7
LST12-12bT	32.5	62.6	2.2	0.9		3.6			5.6			##
LST12-BS-13	33.2	40.5	7.1	9.6	1.5	28.4	3.4		1.2	2.0	4.6	
LST12-BS-14	34.2	7.0	2.4	3.5		18.1			0.8		4.1	
LST12-16bH	35.0	55.2	2.8	3.8	0.7	31.1	2.9		0.7	0.9	0.6	
LST12-16bT	35.0	55.5	2.9	4.6	0.7	30.0	2.7		0.5		1.3	
LST12-5	35.1	65.0	4.7	1.3		11.2	3.5		8.8	tr.	5.1	
LST12-BS-17	35.5	74.0	5.8	4.2		12.1			0.5		3.3	
LST12-BS-18	35.9	41.3	7.1	9.1	1.4	29.7	3.1		1.0	1.8	4.6	
LST12-6	37.0	48.1	2.8	0.5		0.6	tr.	1.0	46.7			
LST12-19b	38.0	36.4	1.4	tr.		8.5		1.0	51.9			
LST12-7	39.2	28.8	1.7	0.6		11.7		2.8	54.2			
LST12-20bH	39.8	39.9	1.3					5.4	53.1		tr.	
LST12-20bT	39.8	35.0	1.3					4.0	59.4		tr.	
LST12-8	40.6	26.8	2.1			5.7		1.0	64.3			
LST12-21bH	41.7	18.1	1.1					5.5	74.9		tr.	
LST12-21bT	41.7	27.7	1.2					4.8	66.0		tr.	
LST12-9	42.0	31.8	2.1			4.5		6.1	55.4			
LST12-10	42.2	22.7	1.0			tr.		2.8	73.2			
LST12-23b	44.4	18.0	1.4					1.9	78.3		tr.	
LST12-11	45.0	32.0	1.0	0.9		1.0		2.3	62.4		tr.	
LST12-24bH	46.2	7.8	0.6			tr.		3.0	88.0		tr.	
LST12-24bT	46.2	19.0	tr.	1.4		0.6		6.2	72.0		tr.	
LST12-24bVT	46.2	30.9				0.9		3.5	63.6		0.9	
LST12-12H	47.0	16.0	1.6			0.8		3.6	77.5		0.5	
LST12-12	47.0	15.9	1.3			0.6		2.6	79.1		0.5	
LST12-13H	48.0	14.2	2.2	tr.		0.8		2.6	79.5		0.5	
LST12-13	48.0	11.8	2.1	2.9		0.5		2.5	79.7		0.5	
LST12-25b	49.1	23.4	1.1	0.9		0.8		2.4	71.2		tr.	
LST12-14	50.2	18.0	1.2	tr.				5.5	74.3		tr.	
LST12-15H	51.5	22.7	1.7			1.6		3.4	70.2		tr.	
LST12-15T	51.5	15.2	1.1			0.8		5.1	77.5		tr.	
LST12-26bD	52.0	24.7				4.4		2.0	68.4		tr.	
LST12-26bL	52.0	15.1	tr.			3.8		2.0	78.3		tr.	
LST12-16	52.2	15.2	1.1			0.8		5.1	77.5		tr.	
LST12-BS-27	52.8	40.1	10.0	2.5		26.1			18.2		2.4	
LST12-17	53.8	9.9						0.7	89.2			
LST12-BS-28	53.8	38.1	17.2	4.2		29.7			5.2		4.9	
LST12-29b	54.3	12.5	0.6			tr.			86.1		tr.	
LST12-BS-30	54.6	28.3	10.6	3.6		19.5			31.7		5.9	
LST12-31b	55.2	7.3	1.1					0.5	90.2		tr.	
LST12-18	55.5	17.3		tr.		3.8		0.9	77.1		0.5	
LST12-BS-32	55.7	37.8	12.3	1.0		22.3			8.0		##	
LST12-19	56.1	12.1	1.2	1.2					84.2		1.1	
LST12-BS-33	56.5	52.5	11.9	1.6		30.7			1.9		0.9	

Sample	depth (m)	Quartz (wt.%)	K-feldspar (wt.%)	Plagioclase (wt.%)	Chlorite (wt.%)	K-mica (wt.%)	Kaolinite (wt.%)	Calcite (wt.%)	Dolomite (wt.%)	Siderite (wt.%)	Pyrite (wt.%)	Apatite (wt.%)
LST12-BS-34	57.3	39.8	20.9	1.5		35.4			0.9		1.0	
LST12-35b	57.5	15.3	1.9	1.0					81.4			
LST12-BS-36	58.1	28.1	37.7	2.5		30.2			0.9		0.6	
LST12-38b	59.5	4.7	tr.	0.7		2.6			91.3		tr.	
LST12-20	60.0	1.6	0.8					1.8	95.4			
LST12-BS-39	60.5	59.2	12.1	2.5		21.7			3.3		1.0	
LST12-BS-40	61.2	76.4	4.1	2.2		14.6			2.1		tr.	
LST12-21	62.0	13.2	1.8			4.8		1.4	78.4			
LST12-22	63.0	5.0	1.2			2.6		2.1	89.1			
LST12-42b	64.2	13.4	tr.			4.6		1.4	79.9		tr.	
LST12-23	65.0	6.8	1.0			2.2		4.1	85.0		0.9	
LST12-24H	66.0	4.5	1.8			1.7		7.7	83.9		tr.	
LST12-24T	66.0	25.2	1.3			4.5		0.7	68.2			
LST12-25	67.0	8.2	1.0			3.1		5.3	81.8		0.5	
LST12-26H	68.0	15.1	0.8	tr.		0.5		2.3	80.8		tr.	
LST12-26T	68.0	24.4	1.0			0.8		2.3	71.0		tr.	
LST12-26	68.0	1.5	tr.			2.5		5.9	89.5			
LST12-43b	69.1	2.9	0.7			3.8		3.8	88.2		0.5	
LST12-27	70.0	2.7	0.9			4.1		4.9	87.1		tr.	
LST12-28	71.0	4.1	tr.			1.5		##	79.5		tr.	
LST12-29	72.0	0.7				2.2		5.2	91.5			
LST12-30	73.0	5.2	0.5			1.7		2.9	89.3		tr.	
LST12-44b	74.0	0.9				3.2		5.3	9.0		tr.	
LST12-31	75.0	0.7				1.4		5.3	92.2			
LST12-32H	75.5	0.5	tr.			tr.		4.2	94.3		tr.	
LST12-32T	75.5	54.4						##	7.1		tr.	
LST12-33	76.0	1.0	tr.			2.7		5.3	89.6		tr.	0.8
LST12-34	77.0	2.4				1.4		2.5	91.2			2.4
LST12-45bG	78.8	0.5				4.4		0.6	91.2		0.5	2.5
LST12-45bP	78.8	1.0				3.8		5.8	89.1		tr.	
LST12-35	79.0	0.7	tr.			2.5		9.4	81.9		0.5	4.6
LST12-46bD	79.1	1.0				4.0		7.0	86.9		0.8	
LST12-46bS	79.1	9.2	1.1			10.7		1.9	73.1		3.4	tr.
LST12-36	80.0	3.0	0.6			2.9		8.9	83.8			0.6
LST12-37	81.0	1.5	tr.			2.4		6.8	87.5			1.1
LST12-47b	81.8	1.6	0.5			2.5		5.8	87.1			2.1
LST12-38	83.0	0.9	tr.			2.3		6.4	88.9			0.8
LST12-39	84.0	0.9	1.1			6.6		2.6	86.0			2.6
LST12-40	85.0	2.7	tr.			1.5		3.1	91.9			tr.
LST12-41	86.0		0.9			8.8		0.8	86.9			2.4
LST12-48b	86.9	1.5	0.7			2.6		2.2	92.4		tr.	
LST12-42	87.9	1.2	tr.			1.9		5.0	91.6			
LST12-43	88.0	2.5	tr.			2.6		3.2	91.0			
LST12-44	89.0	0.5				0.9		4.1	94.3			
LST12-45	90.0	0.9	tr.			2.2		3.8	89.1			3.4
LST12-46	91.0	1.3	0.5			2.4		1.2	94.3			
LST12-47	92.0	1.2	0.5			2.3		2.2	93.5			
LST12-49b	92.4	0.7				1.8		1.4	95.8			
LST12-50b	93.2	0.6				2.0		2.0	94.3		tr.	tr.
LST12-48	94.0	0.5	tr.			tr.		3.9	94.7			
LST12-49	95.0	1.1	0.8			0.8		3.1	93.6		0.6	
LST12-50	96.0	9.6	0.9			4.8		1.1	82.7		0.7	
LST12-51b	97.0	3.7	1.0			2.5		1.9	90.6		tr.	
LST12-51	97.0	7.6	1.0			6.3		0.6	83.8		0.5	
LST12-52b	98.0	3.7	1.0			2.5		1.9	90.6		tr.	
LST12-52	98.7	14.7	1.1			6.9		tr.	75.9		0.8	
LST12-53	99.0	6.6	1.1			4.6		1.7	85.3		0.5	
LST12-53bG	100.0	1.1	0.6			3.7		2.4	90.5	0.5	0.8	
LST12-53bP	100.0	1.5				6.0		2.4	89.3		0.5	
LST12-53bS	100.0	1.1	1.0	0.6		13.0		8.0	75.2		1.1	
LST12-54H	100.0	2.5	0.6			1.2		##	74.0			
LST12-54T	100.0	2.3	0.9			1.0		3.6	91.1		0.9	
LST12-55H	101.0	3.7	0.6			tr.		tr.	94.0			1.1
LST12-55T	101.0	2.0	1.2	tr.		2.9		1.7	91.6		tr.	
LST12-54b	101.9	2.7	1.0			4.6		1.7	89.3		0.5	
LST12-56	103.0	3.1	1.2			4.2		1.2	89.8		tr.	
LST12-57	104.0	1.8	0.6			2.2		1.1	93.9		tr.	
LST12-58	105.0	1.0	0.6			3.2		1.2	93.3		tr.	

Sample	depth (m)	Quartz (wt.%)	K-feldspar (wt.%)	Plagioclase (wt.%)	Chlorite (wt.%)	K-mica (wt.%)	Kaolinite (wt.%)	Calcite (wt.%)	Dolomite (wt.%)	Siderite (wt.%)	Pyrite (wt.%)	Apatite (wt.%)
LST12-55b	105.7	3.5	0.6			2.6		4.0	89.0		tr.	
LST12-59	106.9	1.5	tr.			1.8		6.0	9.0			
LST12-60	107.5	2.8	tr.			3.6		0.9	91.7		tr.	
LST12-61	108.0	1.3	1.2	tr.		3.7		5.2	87.6		0.5	
LST12-62	109.0	1.0	2.2	0.6		4.0		1.2	80.6		1.3	
LST12-63	110.0	7.6	1.3	tr.		3.5		1.6	85.5			
LST12-64	111.0	4.8	1.1			2.3		1.6	89.3		1.0	
LST12-65-1	112.1	4.5	1.2			2.6		2.2	88.9		0.7	
LST12-65-2	112.1	4.9	1.3			3.7		2.1	87.2		0.6	
LST12-66	113.0	15.5	1.7	tr.		14.1		0.8	67.4			
LST12-67	114.0	14.1	1.3	tr.		7.8		2.3	74.0		tr.	
LST12-68	115.0	5.1	1.5	tr.		4.8		##	77.2		tr.	
LST12-56b	116.5	9.2	2.1			19.1			68.8		tr.	
LST12-69	117.0	12.4	1.7	0.5		20.6	0.6		62.2		1.8	
LST12-57b	117.8	13.6	0.9	1.0		21.7		tr.	61.7		0.9	
LST12-70	119.0	17.3	1.6	1.2		16.8		1.1	62.1			
LST12-71	119.5	27.7	2.2	1.2		18.2		3.1	47.4			
LST12-72	120.0	15.7	3.9	2.0		23.2	1.9	0.8	52.3			
LST12-73	121.0	15.8	2.7	0.7		14.5	1.2	1.1	64.0			
LST12-58b	121.9	21.3	2.2	2.4		19.2		3.0	51.8			
LST12-74	123.0	13.0	4.2	1.5		31.5	1.8	0.7	46.7		tr.	
LST12-75	125.0	16.8	1.5	1.0		9.0	1.1	8.3	62.3			
LST12-76	126.0	14.1	12.5	11.7	4.6	48.4	2.7	0.6	4.8		0.5	
LST12-59b	126.0	24.2	12.8	16.0	4.5	28.9	3.1	0.6	8.9		tr.	
LST12-77	127.8	1.0	1.7	tr.		11.6			76.0			
LST12-60b	128.6	17.5	1.9	6.7		14.8	2.3		56.5			
LST12-60b	128.6	17.9	2.2	7.3		14.6	2.3		55.3			
LST12-78	128.8	14.2	6.3	9.3	2.1	23.5	1.6	0.5	42.2			
LST12-79	130.3	13.1	4.5	7.3	3.9	21.3	0.9	0.7	48.4			
LST12-61bD	131.4	14.2	7.3	12.9	1.7	26.1	1.3	0.7	35.7			
LST12-61bL	131.4	12.9	1.0	0.7		7.5	1.4		76.4			
LST12-80H	132.0	7.4	1.2			1.0			81.1			
LST12-80T	132.0	25.8	8.8	18.3		27.4	2.2	3.3	14.0			
LST12-62bD	132.1	19.6	5.2	11.1	1.3	14.9	1.0	0.8	46.1			
LST12-62bL	132.1	15.8	1.2	4.8		6.4	1.6		7.0			
LST12-81H	133.0	19.6	4.2	10.7		15.5	1.5	0.6	47.8			
LST12-81T	133.0	24.3	10.0	15.2	2.6	25.7	2.7	1.0	18.4			
LST12-63bD	134.0	23.2	15.2	21.1	1.8	30.4	2.4	1.9	3.7			
LST12-63bL	134.0	8.2	1.1			5.8	1.0		83.7			
LST12-82	135.0	17.3	1.4	3.7		7.7	1.1		68.7			
LST12-64bD	135.5	22.1	1.0	17.6	2.6	28.8	3.2	1.6	13.6			
LST12-64bL	135.5	5.1	1.0	0.7		3.7	0.8		87.9		0.6	
LST12-83	136.0	16.0	5.3	9.7	5.8	23.0	2.2	0.8	36.9			
LST12-65bD	136.2	28.2	12.9	19.8	1.5	26.2	3.0	3.4	4.9			
LST12-65bL	136.2	13.3	1.4	tr.		6.1	0.5		78.1			
LST12-66bD	136.9	30.4	11.4	22.0	2.5	25.0	3.4	3.5	1.8			
LST12-66bL	136.9	13.5	0.8	0.9		6.8	1.3		76.5			
LST12-84	137.0	25.6	8.2	15.9	1.8	25.8	2.3	2.6	17.6			
LST12-85H	138.0	4.3	0.9	tr.		5.9	tr.		88.2			
LST12-85T	138.0	19.7	7.1	12.2	3.2	29.5	3.0	2.8	22.1			
LST12-86	138.7	23.8	4.5	17.7	2.2	16.9	2.7	7.0	25.0			

Table 2. Depth and concentrations of selected major and trace elements of the LST12 core samples.

depth (m)	Ca (%)	Fe (%)	Mn (ppm)	Mo (ppm)	U (ppm)	V (ppm)	Al (%)	Re (ppm)
17.2	0.18	4.47	340	0.08	3.3	76	5.41	0.002
25.145	0.11	1.71	342	0.81	5.1	191	4.54	0.009
27.415	0.14	1.58	364	2.87	4.1	141	4.64	0.029
29	2.1	2.13	4342	2.88	2.8	99	4.48	0.052
31.37	3.26	6.26	14260	3.82	9.5	164	2.47	0.019
32.525	3.86	2.17	13752	0.14	1	26	1.81	0.005
34.225	0.19	7.95	652	4.08	4.5	101	2.62	0.027
35.875	0.23	1.4	155	0.6	4.9	78	2.77	0.01
37	10.8	1.81	8021	0.09	0.4	11	0.85	0.002
39.2	13.22	1.7	5530	0.12	0.6	19	2.17	0.002
41.68	19.86	1.21	8064	0.13	0.1	2	0.06	0.002
44.35	17.01	1.18	10543	0.12	0.1	3	0.29	0.002
47	17.22	0.86	7846	0.12	0.3	7	0.95	0.002
49.05	15.66	0.67	6985	0.06	0.1	3	0.39	0.003
51.5	18.22	0.91	10764	0.13	0.2	5	0.27	0.002
52.75	3.7	2.29	786	3.44	4.9	96	4.24	0.015
54.585	5.25	3.06	424	25.66	4.6	261	3.09	0.089
55.695	1.9	9.68	189	14.35	4.5	142	3.25	0.053
57.535	16.91	1.44	2904	0.45	0.4	15	0.43	0.002
59.515	19.59	1.11	1402	0.37	0.2	13	0.27	0.002
62	17.29	0.54	1145	0.27	0.2	6	0.94	0.002
64.2	18.51	0.53	621	0.08	0.2	3	0.7	0.007
66	15.03	0.41	593	0.19	0.3	3	0.75	0.002
68	22.89	0.24	226	0.14	0.2	2	0.34	0.002
70	21.27	0.49	500	0.22	0.4	4	0.74	0.002
72	22.6	0.57	936	0.06	2	3	0.33	0.002
73.95	21.58	0.12	183	0.32	0.2	1	0.34	0.002
75.5	21.07	0.16	416	0.1	0.3	4	0.32	0.02
77	20.71	0.3	334	0.19	0.5	3	0.33	0.002
79	23.13	0.39	355	0.1	0.5	2	0.44	0.002
81	21.5	0.1	95	0.05	0.1	1	0.3	0.002
83	21.9	0.19	178	0.05	0.2	1	0.33	0.002
85	21.4	0.24	175	0.09	0.2	2	0.35	0.002
86.925	20.48	0.4	343	0.08	0.2	5	0.78	0.003
91	21.78	0.16	129	0.08	0.2	2	0.52	0.002
93.17	21.84	0.28	177	0.09	0.1	2	0.4	0.002
95	21.59	0.38	192	0.09	0.1	2	0.48	0.002
96.95	18.29	0.87	314	0.08	0.1	3	0.72	0.002
97.95	20.64	0.5	264	0.05	0.1	3	0.7	0.002
99.985	19.78	0.93	392	0.07	0.3	7	1.3	0.002
101.85	20.42	0.42	991	0.05	0.1	7	0.81	0.002
104	20.67	0.35	512	0.08	0.1	3	0.45	0.002
106.9	21.72	0.24	104	0.05	0.1	2	0.32	0.002
109	17.87	1.56	958	0.08	0.2	25	0.77	0.002
111	20.58	1.02	407	0.15	0.1	15	0.72	0.002
113	16.02	0.43	347	0.05	0.5	17	2.23	0.002
115	21.36	0.5	318	0.19	0.1	6	1.17	0.002
116.49	15.86	0.82	226	0.83	0.3	15	3.11	0.002
119	14.02	1.18	249	0.08	0.3	13	2.94	0.002
121	14.18	1.72	262	0.05	0.1	10	2.71	0.002
123	11.16	1.72	231	0.05	0.2	24	5.22	0.002
125	16.98	2.03	312	0.05	0.1	7	1.64	0.002
127.8	15.58	0.65	310	0.1	0.2	12	2.03	0.002
130.3	11.08	1.66	478	0.05	0.3	19	4.73	0.002
132	17.25	1	397	0.13	0.2	12	1.79	0.002
134.045	2.01	1.52	80	0.54	0.5	23	7.44	0.002
136	9.06	2.35	393	0.06	0.4	32	5.59	0.002
136.85	16.88	1	370	0.05	0.2	16	1.4	0.006
138.7	9.09	1.15	414	0.05	0.4	19	5.11	0.003

Lihtlitsents lõputöö reprodutseerimiseks ja üldsusele kättesaadavaks tegemiseks

Mina, Hele-Riin Juhkama,

1. annan Tartu Ülikoolile tasuta loa (lihtlitsentsi) minu loodud teose

   „Mn-carbonates in carbonate-shale succession in Palaeoproterozoic Lastoursville sub-basin, Gabon“,

   mille juhendaja on Kalle Kirsimäe

   reprodutseerimiseks eesmärgiga seda säilitada, sealhulgas lisada digitaalarhiivi Dspace kuni autoriõiguse kehtivuse lõppemiseni.

2. Annan Tartu Ülikoolile loa teha punktis 1 nimetatud teos üldsusele kättesaadavaks Tartu Ülikooli veebikeskkonna, sealhulgas digitaalarhiivi DSpace kaudu Creative Commonsi litsentsiga CC BY NC ND 3.0, mis lubab autorile viidates teost reprodutseerida, levitada ja üldsusele suunata ning keelab luua tuletatud teost ja kasutada teost ärieesmärgil, alates ***10.06.2022*** kuni autoriõiguse kehtivuse lõppemiseni.

3. Olen teadlik, et punktides 1 ja 2 nimetatud õigused jäävad alles ka autorile.

4. Kinnitan, et lihtlitsentsi andmisega ei riku ma teiste isikute intellektuaalomandi ega isikuandmete kaitse õigusaktidest tulenevaid õigusi.

Hele-Riin Juhkama
01.06.2020